Biomaterials 275 (2021) 120868

Contents lists available at ScienceDirect

Biomaterials

journal homepage: www.elsevier.com/locate/biomaterials

Combined PET and whole-tissue imaging of lymphatic-targeting vaccines in non-human primates

Jacob T. Martin [a,b,1], Brittany L. Hartwell [a,b,1], Sidath C. Kumarapperuma [c,1], Mariane B. Melo [a,b], Diane G. Carnathan [b,d,e], Benjamin J. Cossette [a], Josetta Adams [a], Siqi Gong [f,g,2], Wei Zhang [c], Talar Tokatlian [a,b], Sergey Menis [b,h], Torben Schiffner [b,h], Crystal G. Franklin [c], Beth Goins [c,3], Peter T. Fox [c], Guido Silvestri [b,d,e], William R. Schief [b,h,i,j,k], Ruth M. Ruprecht [g,l,o], Darrell J. Irvine [a,b,j,m,n,*]

[a] Koch Institute for Integrative Cancer Research, Massachusetts Institute of Technology, Cambridge, MA, 02139, USA
[b] Consortium for HIV/AIDS Vaccine Development (CHAVD), The Scripps Research Institute, La Jolla, CA, 92037, USA
[c] Research Imaging Institute, University of Texas Health San Antonio, San Antonio, TX, 78229, USA
[d] Yerkes National Primate Research Center, Emory University, Atlanta, GA, 30322, USA
[e] Emory Vaccine Center, Emory University School of Medicine, Atlanta, GA, 30322, USA
[f] Department of Microbiology, Immunology & Molecular Genetics, University of Texas Health San Antonio, San Antonio, TX, USA
[g] Texas Biomedical Research Institute, San Antonio, TX, 78227, USA
[h] International AIDS Vaccine Initiative Neutralizing Antibody Center, The Scripps Research Institute, La Jolla, CA, 92037, USA
[i] Center for Infectious Disease and Vaccine Research, La Jolla Institute for Immunology, La Jolla, CA, 92037, USA
[j] Ragon Institute of Massachusetts General Hospital, Massachusetts Institute of Technology and Harvard University, Cambridge, MA, 02139, USA
[k] Department of Immunology and Microbiology, The Scripps Research Institute, La Jolla, CA, 92037, USA
[l] Department of Microbiology, Immunology & Molecular Genetics, University of Texas Health San Antonio, San Antonio, TX, 78229, USA
[m] Departments of Biological Engineering and Materials Science and Engineering, Massachusetts Institute of Technology, Cambridge, MA, 02139, USA
[n] Howard Hughes Medical Institute, Chevy Chase, MD, 20815, USA
[o] Department of Biology, University of Louisiana at Lafayette, Lafayette, LA, 70503, USA

ARTICLE INFO

Keywords:
Vaccines
HIV
Nanoparticles
PET imaging
Fluorescence imaging
Non-human primates

ABSTRACT

Antigen accumulation in lymph nodes (LNs) is critical for vaccine efficacy, but understanding of vaccine biodistribution in humans or large animals remains limited. Using the rhesus macaque model, we employed a combination of positron emission tomography (PET) and fluorescence imaging to characterize the whole-animal to tissue-level biodistribution of a subunit vaccine comprised of an HIV envelope trimer protein nanoparticle (trimer-NP) and lipid-conjugated CpG adjuvant (amph-CpG). Following immunization in the thigh, PET imaging revealed vaccine uptake primarily in inguinal and iliac LNs, reaching distances up to 17 cm away from the injection site. Within LNs, trimer-NPs exhibited striking accumulation on the periphery of follicular dendritic cell (FDC) networks in B cell follicles. Comparative imaging of soluble Env trimers (not presented on nanoparticles) in naïve or previously-immunized animals revealed diffuse deposition of trimer antigens in LNs following primary immunization, but concentration on FDCs in pre-immunized animals with high levels of trimer-specific IgG. These data demonstrate the capacity of nanoparticle or "albumin hitchhiking" technologies to concentrate vaccines in genitourinary tract-draining LNs, which may be valuable for promoting mucosal immunity.

* Corresponding author. Koch Institute for Integrative Cancer Research, Massachusetts Institute of Technology, Cambridge, MA, 02139, USA.
E-mail address: djirvine@mit.edu (D.J. Irvine).
[1] Equal contributions.
[2] Current affiliation: New Iberia Research Center, Univ. Of Louisiana at Lafayette, Lafayette, LA, USA.
[3] Deceased.

https://doi.org/10.1016/j.biomaterials.2021.120868
Received 11 February 2021; Received in revised form 27 April 2021; Accepted 28 April 2021
Available online 14 May 2021

1. Introduction

Unlike oral or systemically-administered drugs, the majority of licensed vaccines are administered as parenteral injections into the muscle or skin, and are thought to act in a local, regionalized manner at the lymph nodes draining the injection site. Primary immune responses require antigen to be delivered to lymph nodes, where antigen-specific activation of naïve T cells and B cells is orchestrated. Both T and B cell responses are sensitive to the amount of antigen accumulating in lymph nodes [1–3]. In addition, preferential transport of vaccine adjuvants into lymphatics rather than the blood circulation is critical to avoid systemic side effects [3]. Thus, biodistribution plays a key role in both the safety and efficacy of vaccines. Responding T cells and B cells are also programmed in lymph nodes in a tissue-specific manner: lymphocytes activated in gut-associated lymphoid tissues are induced to express gut homing adhesion and chemokine receptors, activation in skin-draining lymph nodes leads to skin-homing lymphocytes, and activation in lung-draining lymph nodes primes lymphocytes that traffic to the respiratory mucosa [4–6]. This tissue-specific programming extends also to lymphocyte effector functions such as class switching of B cells to produce IgA in mucosa-draining lymph nodes [7–9]. Thus, targeting vaccines to lymph nodes draining mucosal sites may be an effective strategy for optimal protection at these sites of pathogen entry [10].

The transport and localization of vaccines within lymph nodes also has significant implications for the resulting immune response. Antigens and adjuvant compounds carried into lymph can be captured by macrophages in the subcapsular sinus or medullary regions of the lymph node, transported to follicular dendritic cells (FDCs) localized within B cell follicles, or trafficked into collagen conduits that enter the follicles or the deeper T cell regions of the lymph node [11–13]. Intranodal antigen trafficking is particularly important in the humoral immune response: Activated B cells enter germinal centers (GCs) where they will cyclically proliferate, undergo somatic hypermutation of their antigen receptors, and interact with follicular helper T cells (Tfh). Antigen must be efficiently captured in the GC to support affinity maturation of the antibody response, which can persist for weeks to months following a single immunization [14,15].

These issues have motivated increasing efforts to understand factors impacting immunogen and adjuvant biodistribution. Physical size plays an important role in dictating whether parenterally-injected compounds clear from tissues by entering blood versus lymphatic vessels [16,17]. Thus, vaccines formulated as particulates [18–21], modified to bind to lymph-trafficking albumin [3], or engineered to bind tightly to the common vaccine adjuvant alum [22,23] show reduced dissemination into the blood and enhanced lymph node accumulation. Within lymph nodes, particulate antigens that are recognized by natural IgM or trigger spontaneous complement activation are shuttled in a complement-dependent manner to the FDC network, in a manner also dependent on particle size [24,25], while soluble glycoproteins can be captured by interfollicular macrophages and dendritic cells (DCs) via scavenger receptors [26]. We recently reported that nanoparticle forms of densely-glycosylated HIV Env immunogens are recognized by mannose binding lectin, leading to complement activation through the lectin pathway and subsequent rapid trafficking to FDCs within lymph nodes [27]. However, strategies for lymph node targeting and modulation of antigen trafficking have to date been primarily studied in small animal models, and insight into vaccine biodistribution in large animals that would more closely approximate the setting of human immunization, especially on a whole-animal level, remains limited.

Here we combined dual positron emission tomography (PET), whole tissue light sheet microscopy, and traditional histology methods to visualize the fate of HIV Env subunit vaccines from the whole-animal to microscopic levels in rhesus macaques, the most relevant preclinical model for HIV vaccine development. We analyzed the biodistribution of a vaccine incorporating two distinct technologies for targeting immunogen and adjuvant to regional lymph nodes: linkage of a molecular adjuvant, CpG DNA, to an albumin-binding lipid moiety (to exploit "albumin hitchhiking" for lymph node targeting [3,28]), and formulation of a stabilized HIV Env gp140 trimer, either as a soluble trimer or as a self-assembled trimer-nanoparticle, favoring LN trafficking through physical size. Using PET imaging, we traced vaccine localization following injection at a subcutaneous site selected to favor vaccine accumulation in inguinal and iliac lymph nodes that drain the vaginal tract and rectum [29,30], of interest for promoting mucosal immunity to HIV. Guided by *ex vivo* PET analysis of necropsied lymph nodes, we further imaged the localization of fluorescently-labeled antigen and adjuvant in draining lymph nodes in both intact whole lymph nodes and sectioned tissues. We analyzed the localization of vaccine at both early (two days post immunization) and later (7 days p. i.) time points, to gain insights into how the physical form of immunogen and adjuvant influence localization within lymphoid tissues.

2. Materials and methods

2.1. Immunogen synthesis

MD39. MD39, a BG505 SOSIP trimer, was prepared as previously described [31,32]. Briefly, trimer genes containing *C*-terminal His-tags were co-transfected with human furin at a 2:1 trimer:furin DNA ratio using 293fectin into FreeStyle 293-F cells (ThermoFisher). Supernatants were harvested five days post transfection by centrifugation and purified by affinity chromatography using HisTrap HP columns (GE Healthcare) followed by size-exclusion chromatography (SEC) using a S200 Increase column (GE Healthcare). Trimer molecular weight was confirmed by SEC multi-angle light-scattering (SECMALS) using DAWN HELEOS II and Optilab T-rEX instruments (Wyatt Technology). MD39-NPs, a nanoparticulate fusion of MD39 and ferritin from the hyperthermophilic archaeal anaerobe *Pyrococcus furiosus*, were produced and purified by lectin chromatography and SEC as previously described [27]. Particle formation was assessed by SECMALS and by staining MD39-8mer with 2% uranyl formate, gridding and imaging by negative stain electron microscopy on a Philips CM100 TEM with a Soft Imaging Systems MegaView III CCD and SIA model 12C CCD cameras.

MD39-NP. For PET/MRI imaging, MD39-ferritin was labeled with copper-chelating agent DOTA–NHS–ester (Macrocyclics) in 0.1 M sodium phosphate buffer (pH 7.3) previously treated with Chelex 100 chelating resin (BioRad), and allowed to react overnight at 4 °C. The labeled product was purified using a Sephadex G-25 PD-10 Desalting column (GE) and stored at −80 °C until use. For fluorescence imaging, MD39-ferritin or soluble MD39 were labeled with Alexa Fluor 647 (AF647) antibody labeling kits (Thermo Fisher Scientific) and unreacted dye was removed according to the manufacturer's instructions. Labeling conditions were optimized to achieve a mean labeling of ~1.1 AF647 dyes per MD39 trimer in each case.

2.2. Adjuvant synthesis

Amph-CpG. DOTA-labeled amph-CpG 7909 adjuvant used for PET/MRI imaging studies (5'–Diacyl–T-*s*-dC-dG-T-*s*-dC-dG-T-*s*-T-*s*-T-*s*-T-*s*-dG-*s*-T-*s*-dC-dG-T-*s*-T-*s*-T-*s*-T-*s*-dG-*s*-T-*s*-dC-dG-T-*s*-dT–C6Amino–DOTA-3′, where 's' denotes phosphorothioate linkages) was prepared by solid phase synthesis by OligoFactory (Holliston, MA). The lipid moiety used to produce amph-CpG 7909 was bisstearamide CEP diacyl monomer, provided by Berry and Associates (Dexter, MI). The product was stored at −80 °C until use. Similarly, 3′-terminal amine-modified amph-CpG7909 used for fluorescence imaging (5'–Diacyl–T-*s*-dC-dG-T-*s*-dC-dG-T-*s*-T-*s*-T-*s*-T-*s*-dG-*s*-T-*s*-dC-dG-T-*s*-T-*s*-T-*s*-T-*s*-dG-*s*-T-*s*-dC-dG-T-*s*-dT–C6Amino-3′) was also synthesized by OligoFactory. This material was labeled with NHS-rhodamine (Thermo Fisher Scientific) according to the manufacturer's instructions, then purified using a PD-10 desalting column (GE).

Saponin nanoparticles. The saponin nanoparticle adjuvant used for antigen comparison and boost immunization studies was an ISCOM-like nanoparticle comprised of self-assembled cholesterol, phospholipid, and Quillaja saponin prepared as previously described [27]. All synthesis was performed under sterile conditions with sterile reagents. Briefly, 10 mg each of cholesterol (Avanti Polar Lipids 700,000) and DPPC (Avanti Polar Lipids 850,355) were dissolved separately in 20% MEGA-10 (Sigma D6277) detergent at a final concentration of 20 mg/mL and 50 mg Quil-A saponin (InvivoGen vacquil) was dissolved in deionized water at a final concentration of 100 mg/mL. Next, DPPC solution was added to cholesterol followed by addition of Quil-A saponin in rapid succession and the volume was brought up with PBS for a final concentration of 1 mg/mL cholesterol and 2% MEGA-10. The solution was allowed to equilibrate at 25 °C overnight, followed by 5 days of dialysis against PBS using a 10 k MWCO membrane. The adjuvant solution was then filter sterilized using a 0.2 μm Supor syringe filter, concentrated using 50 k MWCO centricon filters, and further purified by FPLC using a Sephacryl S-500 HR size exclusion column. Each adjuvant batch was finally characterized by negative stain TEM and DLS to confirm uniform morphology and size and validated for low endotoxin by Limulus Amebocyte Lysate assay (Lonza QCL-1000). Final adjuvant concentration was determined by cholesterol quantification (Sigma MAK043), assuming lipids and saponin incorporated into the particles in the same molar ratios as initially added to the synthesis. Doses of saponin adjuvant are reported in terms of the mass of saponin.

2.3. Radiochemistry

^{64}Cu-chloride obtained from the University of Wisconsin-Madison was neutralized with previously Chelex®-treated 1 M ammonium acetate buffer (Sigma) and the pH was adjusted to approximately 5.5. Radioactivity was measured using a Capintec CRC®-25 R dose calibrator. An aliquot of ^{64}Cu-chloride (~370 MBq) was mixed with DOTA-MD39 nanoparticles (53 μg, 1.06 mg/mL) in ammonium acetate buffer (pH 5.5) and incubated for 1 h at 40 °C in a circulating water bath. The reaction mixture was then loaded on to Zeba® desalting spin columns (40 kD MWCO, Thermo Fisher) and eluted with phosphate buffered saline (PBS, Thermo Scientific). The purity of eluted ^{64}Cu-DOTA-MD39 nanoparticle sample was determined by instant thin layer chromatography (iTLC). As ferritin itself has the potential to bind to metal ions, we carried out initial tests of ^{64}Cu binding to MD39-ferritin particles with vs. without DOTA labeling, and found that DOTA-MD39-ferritin bound to 8.5 μCi/μg protein, while MD39-ferritin bound only 1.8 μCi/μg protein. Thus, while there is some binding by ferritin itself, it was only ~20% of the labeling that could be achieved using DOTA tagging. An aliquot of ^{64}Cu-DOTA-MD39 NP (25 μg mL^{-1} per administered dose) was mixed with AF647-MD39-NP (25 μg mL^{-1}), amph-CpG7909 (125 μg mL^{-1}), and rhodamine-amph-CpG7909 (125 μg mL^{-1}) to prepare the vaccine formulation (38–148 MBq in 1 mL of PBS). Amph-CpG-DOTA was loaded with ^{64}Cu by the same procedure. Then an aliquot of ^{64}Cu-DOTA-amph-CpG (125 μg mL^{-1} per administered dose) was mixed with rhodamine-amph-CpG7909 (125 μg mL^{-1}), MD39-NP (25 μg mL^{-1}), and AF647-MD39-NP (25 μg mL^{-1}) to prepare the vaccine formulation (125–147 MBq in 1 mL of PBS). All formulations were performed under standard aseptic conditions.

2.4. PET imaging studies

PET imaging study immunizations. All animal experiments were performed in accordance with protocols approved by the Institutional Animal Care and Use Committee of UT Health San Antonio and followed National Institutes of Health guidelines for animal care. Indian origin rhesus macaques, *Macaca mulatta*, were anesthetized with ketamine hydrochloride (10 mg kg^{-1}, I.M.) and maintained with isoflurane (1–3%, inhaled) mixed with 100% oxygen using an isoflurane vaporizer. Endotracheal intubation was performed following anesthesia induction. Animals breathed spontaneously throughout the procedure(s). Freshly prepared vaccine formulations were administered subcutaneously in 1 mL of PBS midline at the anterior upper thigh 5 cm below the groin of anesthetized macaques prior to imaging. Group 1 (MD39-NP PET imaging, n = 5) received 50 μg total MD39-NP (25 μg ^{64}Cu-DOTA-MD39-NP + 25 μg AF647-MD39-NP) and 250 μg total amph-CpG (125 μg unlabeled amph-CpG + 125 μg rhodamine-amph-CpG). Group 2 (amph-CpG PET imaging, n = 3) received 50 μg total MD39-NP (25 μg unlabeled MD39-NP + 25 μg AF647-MD39-NP) and 250 μg total amph-CpG (125 μg ^{64}Cu-DOTA-amph-CpG + 125 μg rhodamine-amph-CpG). The animal's body was immobilized in dorsal recumbency within a vacuum sealed veterinary positioner. Radioactive fiducial markers (0.5–2 MBq ^{64}Cu standards) were attached to the animal positioner to assist the PET/MRI co-registration. Body temperature was maintained with a warm air blanket covering the animal (3 M Bair hugger Model 505 warming unit). Continuous physiological parameter monitoring was performed to include measurements of end-tidal P_{CO2}, electrocardiogram, heart rate, and respiratory rate within the 3 T MRI Scanner as well as visual assessment for respiration, movement, and mucosal coloration in the PET Scanner. Upon completion of the PET scan, animals were allowed to fully recover from anesthesia and returned to their housing. All animals underwent 24 h post vaccine injection (p.i) PET scans and some of the animals underwent scans at 3, 48, and 72 h p. i. As well.

MRI Imaging. All MRI studies were performed on a Siemens 3.0 T TIM-Trio MRI scanner (Siemens Healthcare, Malvern, PA, USA) with large 6-channel body matrix phased-array coil and 12-channel spine matrix phased-array coil. The upper and lower body 3D images were acquired separately to cover the whole length of the animal with about 30% overlap between the two image sets. Two to three common fiducial markers were included in each set to assist the PET/MRI co-registration and image merging. The structural T1 images were acquired with a 3D Flash sequence (repetition time/echo time 6.33/1.51 ms, flip angle 10 deg, matrix 512 × 512, coronal, field of view 500 × 250 mm, slice thickness 1.2 mm, 128 slices without gap, 6 averages, accelerate factor 2 GRAPPA, and scan time 366 s).

In vivo PET Imaging. Immediately after the MRI session, animals in the positioner were transferred to the PET scanner bed while maintaining their position. All whole-body PET images were acquired on a CTI EXACT HR + scanner (Knoxville, TN). PET acquisitions were performed in 3D mode in an axial field of view of 15.5 cm with 63–2.5 mm contiguous slices. Emission data were corrected for decay, dead time, scatter, random coincidences and measured photon attenuation (with ^{68}Ge/^{68}Ga transmission scans) using the scanner software (ECAT version 7.2, CTI PET Systems, Knoxville, TN). Corrected image data were reconstructed using OSEM with 4 iterations and 16 subsets, applying a matrix size of 256 × 256 and a 5 mm FWHM standard Gaussian filter. All acquired image data were archived on an XNAT-powered data archival system for post-acquisition data analysis.

Necropsy, Ex vivo PET Imaging, and Tissue Preservation. At the end of the last PET imaging session, animals were humanely euthanized with 100 mg kg^{-1} euthanasia solution (Euthasol®, i. v.) and the necropsy was performed by an experienced veterinary pathologist. Relevant harvested tissues (e.g. lymph nodes) were re-scanned using the PET imaging protocol described above. Isolated tissues were preserved in freshly prepared paraformaldehyde-lysine-periodate fixative (PLP) and stored at 4 °C for further analysis by optical microscopy.

PET/MRI Data Analysis. PET and MRI data analyses and PET/MRI co-registrations were performed using Multi-Image Analysis GUI (MANGO, Research Imaging Institute, UT Health San Antonio). Decay-corrected (to vaccine injection time) PET images were normalized by injected doses and body weight to produce Standardized Uptake Value (SUV) maps. Regions of Interest (ROIs) were drawn on target tissues by placing spherical outlines, free hand outline drawing, and/or by signal thresholding of tissue contours on the SUV maps. Statistical calculations were performed on these ROIs to determine SUV_{max}, SUV_{mean}, and SUV_{sum}. Three-dimensional (3D) image data were presented as color-

coded maximum intensity projections (MIPs) of the SUV_{max} maps. Distal lymph node analysis was performed by drawing 3D ROIs for the injection site and most distal lymph node with significant detectable signal, which were then projected to a 3D surface-rendered PET image. A straight line was drawn connecting the SUV_{max} points of the injection site and the relevant lymph node on the 3D image to measure distance traveled by the vaccine.

2.5. Fluorescent immunogen immunization studies

Fluorescent antigen immunization studies were carried out at the Yerkes National Primate Research Center (YNPRC) at Emory University. All animal experiments were performed in accordance with protocols approved by the Institutional Animal Care and Use Committee of Emory University and followed National Institutes of Health guidelines for animal care. For soluble MD39 trimer vs. MD39-NP comparisons, groups of rhesus macaques were immunized on day 0 with 50 μg AF647-conjugated MD39 soluble trimer and 187.5 μg saponin adjuvant in the right and left inner thighs (same location as the PET imaging studies), or 50 μg AF647-MD39-NP and 187.5 μg saponin adjuvant in right and left inner thighs. Animals were sacrificed and lymph nodes collected for analysis two or seven days post immunization. For studies assessing the impact of pre-existing antibodies on immunogen trafficking, a group of macaques previously immunized with a related SOSIP trimer according to the schedule shown in Fig. S8A were immunized with 50 μg AF647-MD39 soluble trimer and 187.5 μg saponin adjuvant in the right and left inner thighs. Animals were sacrificed and lymph nodes collected for analysis two or seven days post immunization.

2.6. Ex vivo tissue fixation

All NHP LNs were harvested and immediately placed in PLP buffer (pH 7.4 50 mM PBS + 100 mM lysine, 1% paraformaldehyde, 2 mg/mL sodium periodate) for fixation. After 4–5 days at 4 °C, tissues were washed and stored in PBS with 0.05% sodium azide at 4 °C until imaging.

2.7. Whole organ fluorescence measurement

Total antigen signal within LNs was measured by placing the tissues directly on the glass scanning surface of a Typhoon FLA 9500 biomolecular imager (GE Healthcare Life Sciences) and imaging using a 635 nm excitation laser and ≥665 nm long-pass filter (for Alexa Fluor 647) or 532 nm excitation laser and ≥575 nm long-pass filter (for rhodamine). The integrated signal density corresponding to AF647-MD39 or rhodamine-amph-CpG in each LN was calculated using ImageJ and plotted using GraphPad Prism 8.

2.8. Whole organ clarification

Selected LNs were clarified via a hybrid protocol, merging aspects of iDISCO [33] and CUBIC [34] organ-clearing methods. The LNs were first delipidated based on the iDISCO methanol incubation protocol: Tissues were washed in water for 1 h, then 20% methanol in water for 2 h. A series of step increases in methanol percentage (40%, 60%, 100%, 100%) followed, each step for 2 h. The LNs were then placed into 2:1 MeOH:DCM overnight, and the next day were rehydrated with the following series of methanol solutions for 2 h each: 100%, 100%, 80%, 60%, 40%, 20%, 0%, 0%. Next, the LNs were placed into 10–20 mL of a 1:1 mixture of CUBIC-R solution for 1 day, followed by at least 20 mL of undiluted CUBIC-R for 2 days or as long as needed for adequate clarification. Larger organs were moved into a fresh 20 mL of CUBIC-R solution to ensure that the refractive index of the solution would not be significantly lowered by residual water in the tissue.

2.9. Light sheet microscopy

Clarified LNs were imaged in CUBIC-R solution using a LaVision Ultramicroscope II Light Sheet Microscope at 1.25x optical zoom. The Alexa Fluor 647-labeled antigen was imaged using the 640 nm laser and the rhodamine-labeled adjuvant was imaged using the 561 nm laser at 100 ms exposure time on an Andor Neo camera. Snapshots and movies were generated using the 3D viewer in the FIJI package of ImageJ.

2.10. Immunofluorescence staining

Selected LNs were embedded in 3% low melting temperature agarose (Sigma-Aldrich), and then sliced into 350 μm-thick sections using a vibratome. The slices were blocked and permeabilized overnight in PBS with 5% mouse serum, 5% rat serum, and 0.2% Triton-X-100, followed by staining for 3 days at 37 °C with 1:100 dilutions of Brilliant Violet 421-labeled mouse anti-human CD35 clone E11 (BD Biosciences) and Alexa Fluor 488-labeled mouse *anti*-Ki67 clone B56 (BD Biosciences) in the same buffer as the blocking/permeabilization step. Stained slices were then washed for 3 days at room temperature with PBS containing 0.2% Tween-20, and then mounted onto glass slides with Prolong Glass antifade mountant (Thermo Fisher Scientific).

2.11. Confocal microscopy

Imaging was performed on either a Leica SP8 or an Olympus FV1200 laser scanning confocal microscope using 10x objectives. Images were analyzed using ImageJ.

2.12. Statistics

Data were statistically analyzed by one-way or two-way ANOVA or by unpaired *t*-test as indicated in the figure captions using GraphPad Prism.

3. Results

3.1. Inner thigh immunization leads to prominent vaccine delivery to inguinal and iliac lymph nodes

We first used PET imaging to visualize the biodistribution behavior of an HIV Env trimer immunogen and molecular adjuvant in rhesus macaques, where each component of the vaccine was prepared in a form designed to promote lymph node targeting. MD39, a hyperstabilized gp140 SOSIP trimer, was fused to an archaeal ferritin, forming a nanoparticle (MD39-NP) presenting eight MD39 trimers [27] with a size (~30 nm diam.) promoting lymphatic trafficking [35]. As an adjuvant, we prepared an amphiphilic lipid-functionalized single-stranded CpG DNA, using a sequence (CpG 7909) selected for stimulation of Toll-like receptor 9 in NHPs and humans [36–38]. This amph-CpG molecule was designed to traffic to lymphatics via binding of the phospholipid tail to endogenous albumin present in interstitial fluid, and in prior studies showed efficient lymph node targeting in mice [3,28]. To enable parallel PET and fluorescence imaging, MD39-NP and amph-CpG were labeled with DOTA as a chelator for ^{64}Cu or with a fluorescent dye. MD39-NP was labeled using N-hydroxysuccinimide Alexa Fluor 647 (AF647) or DOTA, while amph-CpG was labeled at the 3' terminus of the CpG with a single rhodamine or DOTA molecule (Fig. S1A-B). DOTA-labeled molecules were then radiolabeled with ^{64}Cu with greater than 95% purity determined by iTLC (95.40–99.70%, see Methods). ^{64}Cu-loaded DOTA-MD39-NPs were stable for at least 24 h, as evidenced by no drop in radiochemical purity by iTLC and no change in particle size by DLS (Fig. S1C). We expected that amph-CpG-DOTA could be less stable *in vivo*, despite stabilization of the oligonucleotide backbone by phosphorothioate linkages. To assess stability of this conjugate, we incubated ^{64}Cu-loaded amph-CpG-DOTA in rhesus serum for 24 h at 37 °C and then

re-measured radiochemical purity by iTLC. This analysis showed a loss of ~40% of the intact conjugate with release of ^{64}Cu or hydrolysis of the DOTA (Fig. S1D). However, because free ^{64}Cu or ^{64}Cu/DOTA are rapidly cleared *in vivo*, we did not expect this degradation to impact interpretation of the PET scans, and we chose an injected dose to ensure sufficient intact amph-CpG signal for quantification.

For *in vivo* imaging, the injected dose (ID) ranged from 38.48 to 148.74 MBq for ^{64}Cu-DOTA-MD39-NP and 125.06–147.26 MBq for ^{64}Cu-DOTA-amph-CpG (Table S1). As illustrated in Fig. 1A, one group of animals was immunized with ^{64}Cu-DOTA-labeled MD39-NP mixed with fluorescent MD39-NP and fluorescent amph-CpG, while a second group received ^{64}Cu-DOTA-labeled amph-CpG mixed with fluorescent MD39-NP and fluorescent amph-CpG. A secondary goal of this study was to evaluate the ability of vaccines to be targeted to putative reproductive tract/rectum-draining lymph nodes that might promote mucosal immunity. Thus, we administered vaccines subcutaneously in the upper inner thigh of the right leg to assess the potential of targeting vaccine to inguinal, iliac, and possibly deeper internal lymph nodes. All animals underwent whole-body PET and MRI scans at 24 h, followed by an *ex vivo* post-necropsy PET scan to obtain ^{64}Cu signals from isolated lymph nodes and other tissues. Initial pilot immunizations tracking ^{64}Cu signal over 3 days revealed accurately quantifiable PET signals for scans up to 48 h; at 72 h the rapid decay of ^{64}Cu led to low total signals that were unreliable for quantification. Thus, we confined the majority of our analysis to 24–48 h post injection, and necropsied animals after 48 h PET scans for *ex vivo* imaging (Fig. 1A). Dual MRI and PET scanning was performed in order to generate co-registered images that were used to isolate, identify, and quantify regions of interest (ROIs) corresponding to lymph nodes and other tissues (Fig. S2). Following quarantine to allow radioactive decay, the isolated tissues were processed for subsequent histology and whole-tissue fluorescence imaging.

We first imaged the biodistribution of PET-labeled MD39-NPs co-administered with amph-CpG adjuvant. As shown in Fig. 1B, at 24 h post immunization, a substantial pool of MD39-NPs remained in the vicinity of the injection site (approximately 60% of the injected dose). However, clear preferential accumulation of the Env nanoparticles was also observed in ipsilateral inguinal and iliac lymph nodes (Fig. 1B–D and Videos S1 and S2). No antigen signal was detected in contralateral inguinal/iliac LNs, and signals were much lower in systemic tissues such as the gut, heart, liver, or kidneys and not above background in more distal nodes (e.g., axillary) (Fig. 1B–D, Fig. S3A and Videos S1 and S2). At 48 h post immunization, the qualitative biodistribution of MD39-NPs remained unchanged (Fig. S4A). Antigen signals decayed or remained approximately constant in the lymph nodes showing antigen accumulation, and further accumulation at more distal LNs was not detected (Fig. 1D, Fig. S3B). *Ex vivo* PET scans on isolated tissues at 48 h were in concordance with the *in vivo* imaging observations, with significant uptake of the nanoparticle antigen detected in multiple inguinal, external iliac, and common iliac LNs (Fig. 1F). In terms of total injected dose, *ex vivo* PET scans revealed mean accumulations of 2–4% of the antigen in the proximal draining lymph nodes (Fig. S3C-D).

Supplementary video related to this article can be found at doi:10.1016/j.biomaterials.2021.120868.

We next visualized dissemination of DOTA-labeled amph-CpG adjuvant using PET imaging. Amph-CpG appeared to clear from the immunization site more rapidly than the Env trimer nanoparticles, with only 25% of the injected dose remaining at the injection site 24 h after immunization (Fig. 2A). Clear accumulation in inguinal and iliac lymph nodes was visualized in the live animals (Fig. 2B–C, Fig. S5A, and Videos S3 and S4). The albumin-binding adjuvant also trafficked further than MD39-NPs, with adjuvant signal detected in common and internal iliac LNs, and even low levels of signal in para-aortic nodes up to 17 cm away from the immunization site (Fig. 2D and Fig. S6). This more distal dissemination of amph-CpG up the LN chain was confirmed by *ex vivo* imaging of tissues at 48 h (Fig. 2F). Similar to the findings from imaging MD39-NP, 2–5% of the injected dose accumulated in the proximal draining nodes (Fig. S5B-C). At 48 h post immunization, the qualitative biodistribution of amph-CpG remained unchanged (Fig. S4B). Altogether, these data demonstrate that s. c. inner thigh immunization was effective for rapidly delivering vaccine antigen and adjuvant to inguinal and iliac lymph nodes.

Supplementary data related to this article can be found online at doi:10.1016/j.biomaterials.2021.120868.

3.2. HIV Env trimer nanoparticles concentrate in the follicles of macaque lymph nodes

In the experiments described above, each of the radiolabeled vaccines was co-administered with fluorescently labeled MD39-NP and amph-CpG to permit subsequent fluorescent imaging. This enabled us to examine the uptake of MD39-NP and amph-CpG within tissues recovered from the PET-imaged NHPs to define their localized biodistributions within the draining lymph nodes. We selected iliac and inguinal LNs that were positive for antigen and/or adjuvant signal based on both *ex vivo* PET scans and fluorescence signals collected with a high-throughput flatbed Typhoon fluorescence scanner. Vaccine fluorescence signals showed the same patterns of LN accumulation as observed for *ex vivo* PET signals for both MD39-NP and amph-CpG, indicating consistent trafficking behavior from PET- or fluorophore-labeled vaccine (Fig. S7A-D). Additionally, there was a strong correlation between the fluorescence signal of MD39-NP and amph-CpG in all lymph nodes (Fig. 3A). We first sectioned selected LNs that showed median levels of antigen accumulation by *ex vivo* PET into 100 μm thick slices. To identify B cell follicles, we immunostained for CD35, a marker characteristic of follicular dendritic cells (FDCs), and imaged slices by confocal microscopy. Env trimer NPs and amph-CpG showed very distinct patterns of accumulation in draining nodes: While the CpG adjuvant signal localized in the deeper parenchyma of the lymph nodes and surrounding some follicles, MD39-NP signal was observed in a half-moon-like distribution ringing the FDC networks of follicles (Fig. 3B–C). As expected from the PET imaging, no signal for either antigen or adjuvant were detected in contralateral LNs (Fig. 3B). We previously observed MD39-NP concentration in follicles in mice [27], but in mice the trimer nanoparticles accumulated more uniformly across the FDC network, whereas in NHPs we observed peripheral accumulation around the rim of the follicles.

To gain further insight into antigen and adjuvant distribution within the tissues, we established methods to clear whole macaque lymph nodes for whole-tissue imaging by light sheet microscopy. In preparation for imaging the selected samples, we evaluated a variety of published tissue clearing protocols for their capacity to enable high signal-to-noise imaging in the wavelengths used for the antigen and adjuvant dye labels with minimal autofluorescence on fixed NHP LN tissues. We found that an optimal protocol involved removing lipids with organic solvents [33], followed by rehydrating the tissue and raising the refractive index of the solution to match the tissue [34]. As shown for representative iliac (Fig. 3D, Video S5) and inguinal (Fig. 3E, Video S5) lymph nodes, MD39-NPs showed a striking localization in cup-like morphologies, the three-dimensional equivalent of the half-moon patterns observed around the periphery of follicles in the 2D tissue sections. Env NPs were observed in hundreds of follicles across a single lymph node. By contrast, amph-CpG was distributed widely in the LNs and exhibited localization in the lymph node interior/paracortex in some nodes, although also with greater variation by tissue. Altogether, these data suggest that Env NP immunogens are rapidly concentrated in follicles following immunization in NHPs, while CpG adjuvant disperses more broadly in macaque LN tissues.

Supplementary data related to this article can be found online at doi:10.1016/j.biomaterials.2021.120868.

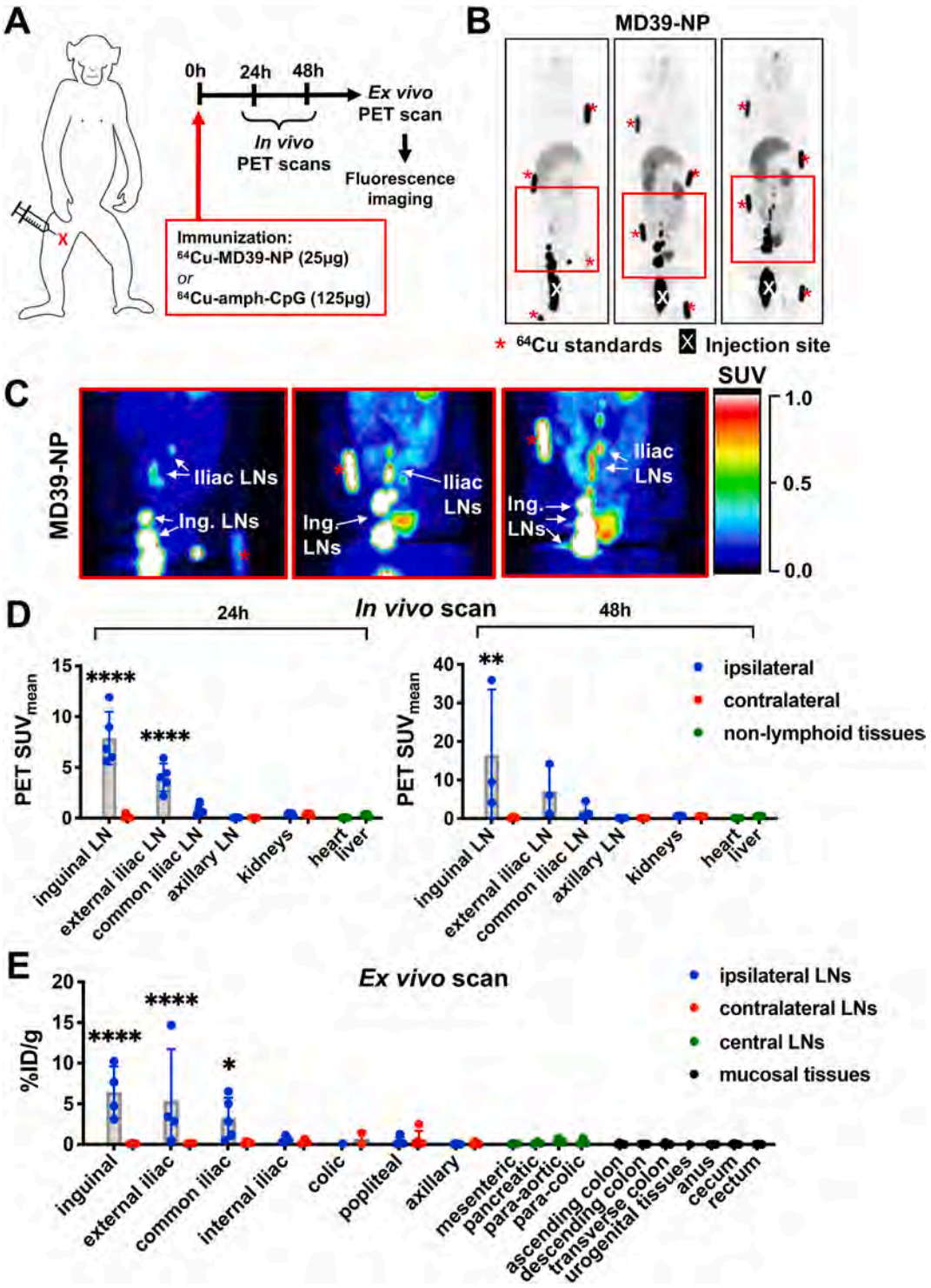

Fig. 1. Accumulation of MD39-NP immunogen in inguinal and iliac lymph nodes of macaques. A) Immunization timeline for PET and MRI imaging studies: Group 1 (n = 5) received 50 μg total MD39-NP (25 μg ^{64}Cu-DOTA-MD39-NP + 25 μg AF647-MD39-NP) and 250 μg total amph-CpG7909 (125 μg unlabeled amph-CpG7909 + 125 μg rhodamine-amph-CpG7909). Group 2 (n = 3) received 50 μg total MD39-NP (25 μg unlabeled MD39-NP + 25 μg AF647-MD39-NP) and 250 μg total amph-CpG7909 (125 μg ^{64}Cu-DOTA-amph-CpG7909 + 125 μg rhodamine-amph-CpG7909). B) Maximum Intensity Projections (MIPs) of representative *in vivo* PET scan at 24 h showing ^{64}Cu-DOTA-MD39-NP signal. "X" denotes injection site, red asterisks indicate fiducial markers. C) Pseudocolor images of boxed areas shown in (B), highlighting drainage to iliac and inguinal lymph nodes (LNs). D) Radiolabeled MD39-NP signal from *in vivo* PET scan of whole animals at 24 h (n = 5) and 48 h (n = 3) quantified as mean standardized uptake value (SUVmean) of gated ROIs; statistical significance compared to liver. E) Radiolabeled MD39-NP signal from *ex vivo* PET scan of isolated tissues post-necropsy at 48 h quantified as percent injected dose (%ID) normalized to excised tissue weight (n = 5); statistical significance compared to non-draining left axillary lymph node. All statistical significance determined by ordinary one-way ANOVA followed by Dunnett's post-hoc test (*$p < 0.05$, **$p < 0.01$, ***$p < 0.001$, ****$p < 0.0001$). (For interpretation of the references to color in this figure legend, the reader is referred to the Web version of this article.)

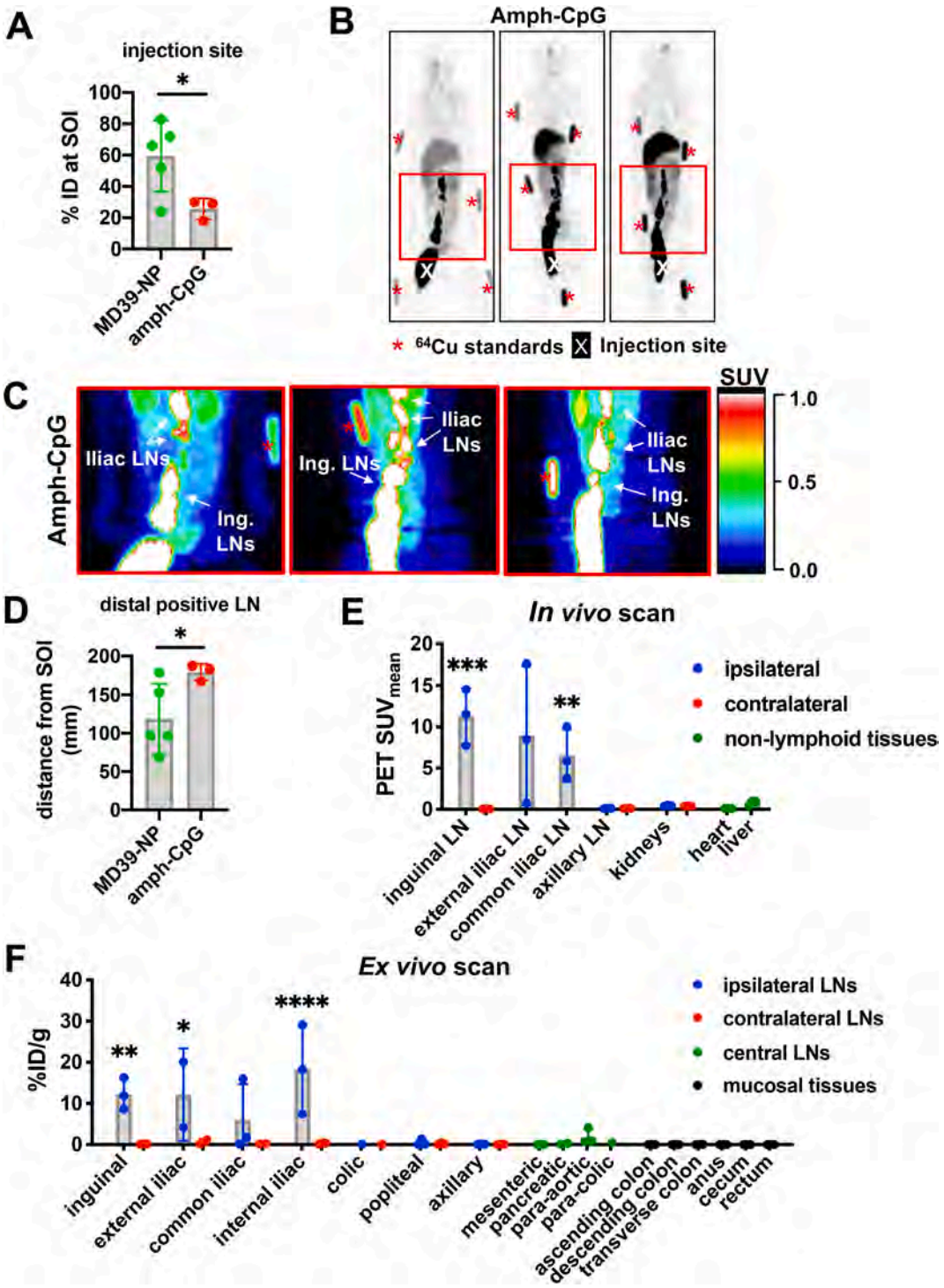

Fig. 2. Accumulation of amph-CpG adjuvant in inguinal and iliac lymph nodes of macaques. A) Percent injected dose (%ID) of ^{64}Cu-DOTA-MD39-NP (n = 5) and ^{64}Cu-DOTA-amph-CpG (n = 3) remaining at site of injection (SOI) at 24 h, determined from *in vivo* PET scan. Statistical significance determined by Welch's *t*-test (*$p = 0.0266$). B) Maximum Intensity Projections (MIPs) of *in vivo* PET scan at 24 h showing ^{64}Cu-DOTA-amph-CpG signal in macaques with region of interest highlighted. "X" denotes injection site, red asterisks indicate fiducial markers. C) Zoomed-in pseudocolor image of ^{64}Cu-DOTA-amph-CpG signal in boxed area shown in (B), highlighting drainage to iliac and inguinal LNs. D) Average distances traveled by ^{64}Cu-DOTA- MD39-NP or ^{64}Cu-DOTA-amph-CpG, determined by calculating distance from SOI to the most distal LN with significant PET signal. Statistical significance determined by Welch's *t*-test (*$p = 0.0390$). E) Radiolabeled amph-CpG signal from *in vivo* PET scan of whole animals at 24 h (n = 4) and 48 h (n = 2) quantified as mean standardized uptake value (SUVmean) of gated ROIs; statistical significance compared to liver. F) Radiolabeled amph-CpG signal from *ex vivo* PET scan of isolated tissues post-necropsy at 48 h quantified as percent injected dose (% ID) normalized to excised tissue weight; statistical significance compared to non-draining left axillary lymph node. Statistical significance determined by ordinary one-way ANOVA followed by Dunnett's post-hoc test (*$p < 0.05$, **$p < 0.01$, ***$p < 0.001$, ****$p < 0.0001$) (n = 3). (For interpretation of the references to color in this figure legend, the reader is referred to the Web version of this article.)

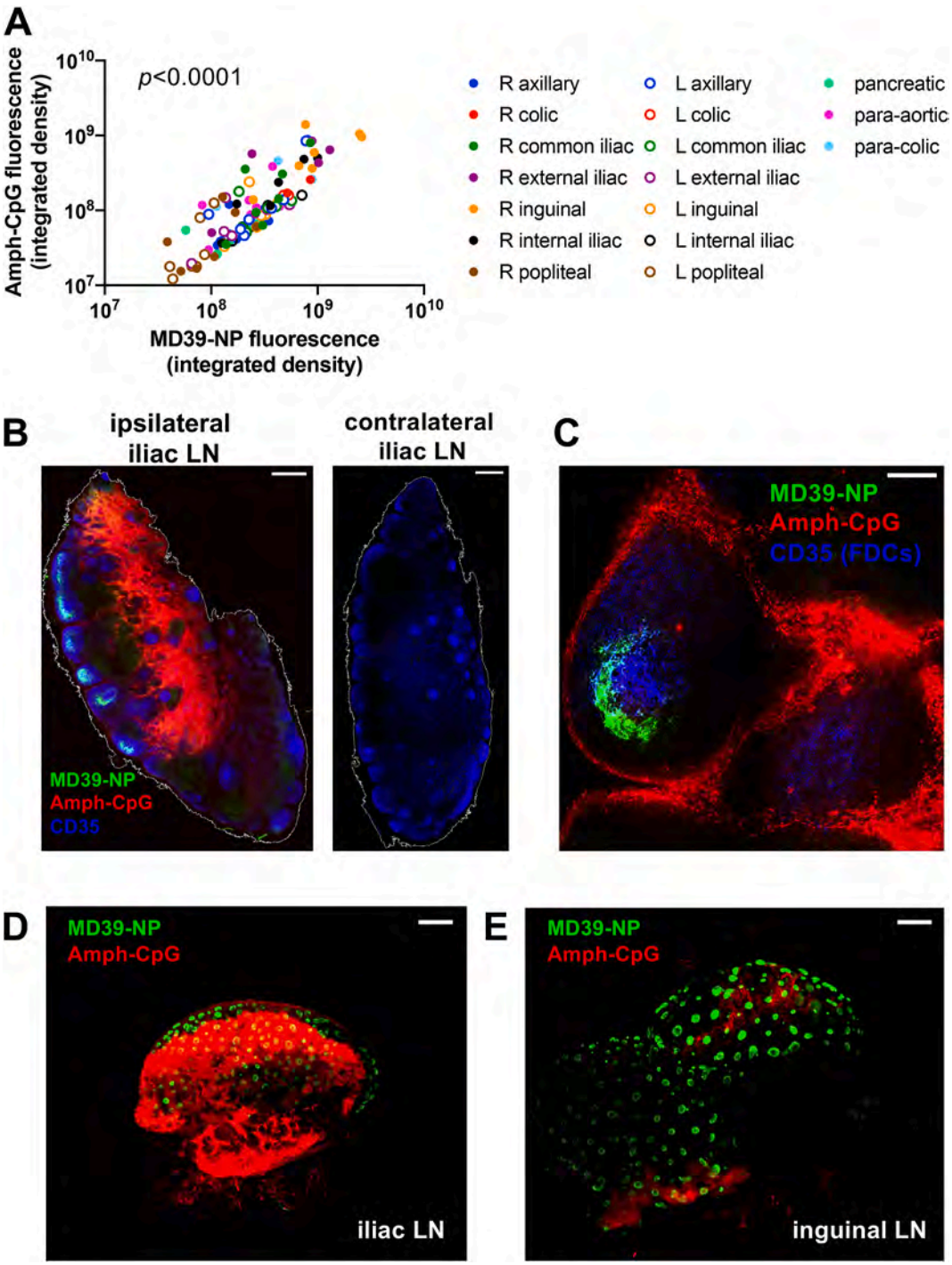

Fig. 3. Distribution and localization of MD39-NP immunogen and amph-CpG adjuvant within lymph nodes. A) Correlations between AF647-MD39-NP and rhodamine-amph-CpG fluorescence signal in individual lymph nodes measured on a Typhoon flatbed scanner ($p < 0.0001$, Pearson's coefficient $r^2 = 0.5893$). B) Comparison of right and left external iliac LNs from a single animal. Scale bar represents 500 μm. C) Higher magnification view of a follicle from the same right external iliac LN shown in panel B. Scale bar represents 100 μm. D-E) Maximum projections of representative whole cleared iliac (D) and inguinal (E) LNs as imaged by light sheet microscopy. Scale bars represent 1 mm.

3.3. Env trimer-nanoparticles exhibit greater LN accumulation and follicular targeting than soluble trimers following primary immunization

Given the striking concentration of MD39-NPs observed both in tissue sections and cleared whole LN organs, we next sought to compare trafficking of the ferritin particle fusion immunogen with free MD39 trimers. Groups of macaques were immunized with Alexa Fluor-labeled MD39 or MD39-NP at an equivalent molar dose of Env trimer, combined with an ISCOM-like saponin adjuvant we have previously found elicits potent humoral responses in NHPs [14,39]. Two or seven days later, animals were necropsied and lymph nodes were collected for analysis (Fig. 4A). Total antigen accumulation in LNs was first assessed by imaging whole fixed LNs on a flatbed laser fluorescence scanner. As NHPs show a variable number of lymph nodes at a given draining site (e.g., inguinal or iliac nodes), we pooled the LNs from each draining site to measure the average total antigen accumulation in distinct drainage

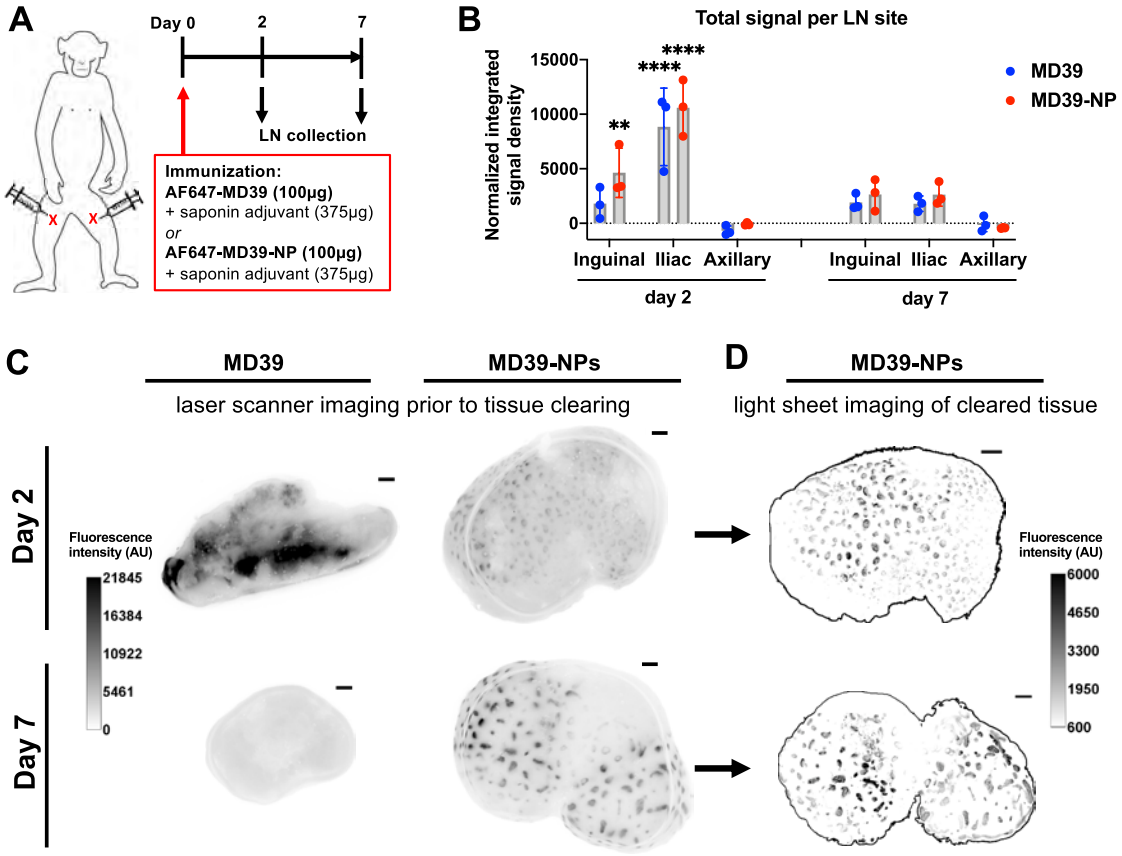

Fig. 4. Env trimer nanoparticles but not free trimer exhibit follicular concentration following a prime immunization. A) Immunization timeline: Rhesus macaques (n = 3/group) were immunized on day 0 with a total dose of 100 μg AF647-MD39 + 375 μg saponin adjuvant *or* 100 μg AF647-MD39-NP + 375 μg saponin adjuvant, administered subcutaneously in both left and right upper inner thighs. Animals were sacrificed and LNs collected two and seven days after immunization. B) Quantification of total fluorescent signal within fixed LNs from each collection site as measured using a fluorescent laser flatbed scanner. Statistical significance compared to non-draining axillary lymph node determined by two-way ANOVA followed by Dunnett's post-hoc test (**$p < 0.01$, ****$p < 0.0001$). C, D) Comparison of LNs from MD39-NP-immunized animals before and after clarification, imaged by laser scanner prior to tissue clearing (C) and by light sheet microscopy after tissue clearing (D), respectively. Light sheet microscopy images are maximum projections through an entire LN stack. Scale bars represent 1 mm.

areas. This analysis revealed that antigen accumulation was readily detectable in inguinal and iliac LNs: On day 2, the amount of MD39 and MD39-NP in iliac LNs, along with MD39-NP in inguinal LNs, was significantly greater than that detected in non-draining axillary LNs (Fig. 4B). By day 7, antigen signal decayed by ~80% in draining LNs (Fig. 4B).

In addition to an integrated measure of total antigen signal, the laser scanner also provided a low-resolution image of the pattern of antigen accumulation in the whole tissues. As shown in Fig. 4C, free MD39 trimer showed a diffuse, inhomogeneous pattern of signal in the fixed tissues, which decayed from day 2 to day 7. By contrast, a clearly punctate pattern of MD39-NP antigen signal was observed at both time points (Fig. 4C). To gain further insight, we next carried out tissue clearing and imaged the same LNs by light sheet microscopy. Strikingly, cleared LNs from animals receiving free trimer showed near-zero antigen signal above background (Video S6). This finding suggests the majority of antigen signal in these lymph nodes may have been localized in lymph fluid in the peripheral sinuses, where it would not be immobilized during fixation and thus would be extracted during the tissue clearing treatment. By contrast, the cup-like follicular concentration of MD39-NPs was observed here as in the prior study (Video S6 and Fig. 4D).

Supplementary data related to this article can be found online at doi:10.1016/j.biomaterials.2021.120868.

To complement the cleared tissue imaging, we also carried out confocal microscopy of 100 μm-thick sections of LN tissues to detect low levels of antigen at higher resolution. Samples were first imaged by the flatbed fluorescence scanner for a low-resolution view of trimer signal, followed by sectioning for confocal imaging of the same samples. As shown in Fig. 5A, two days post immunization, LNs exhibiting diffuse MD39 trimer signal via laser scanner imaging showed detectable antigen signal in the LN parenchyma when imaged at high resolution, albeit at low levels, and dispersed through interfollicular areas, reminiscent of prior reports of trimer distribution in mouse LNs [26,27]. By day 7, soluble trimer signal was decreased but could be detected in FDC networks, and Ki67 staining revealed the initiation of germinal centers (Fig. 5B; note Fig. 5B(iii) highlighting antigen signal as an isolated channel in false color). In contrast, MD39-NP was detected ringing $CD35^+$ follicles at both time points, mirroring the findings from the previous study (Fig. 5C–D). Notably, the trimer nanoparticles accumulated on the side of follicles opposite the prominent Ki67 staining marking areas of B cell proliferation in the dark zone of developing germinal centers, suggesting concentration in the light zone of GCs (Fig. 5D). Thus, Env trimer nanoparticles, but not soluble trimer, efficiently accumulated in follicles as early as 2 days post immunization.

3.4. Soluble Env trimers exhibit follicular targeting in animals with pre-existing anti-Env immunoglobulin

The striking follicular trafficking of MD39-NP mirrors our recent findings of follicular trafficking of the same nanoparticle in mice, which we showed was dependent on mannose binding lectin recognition and complement deposition on the particles [27]. As immune complexes

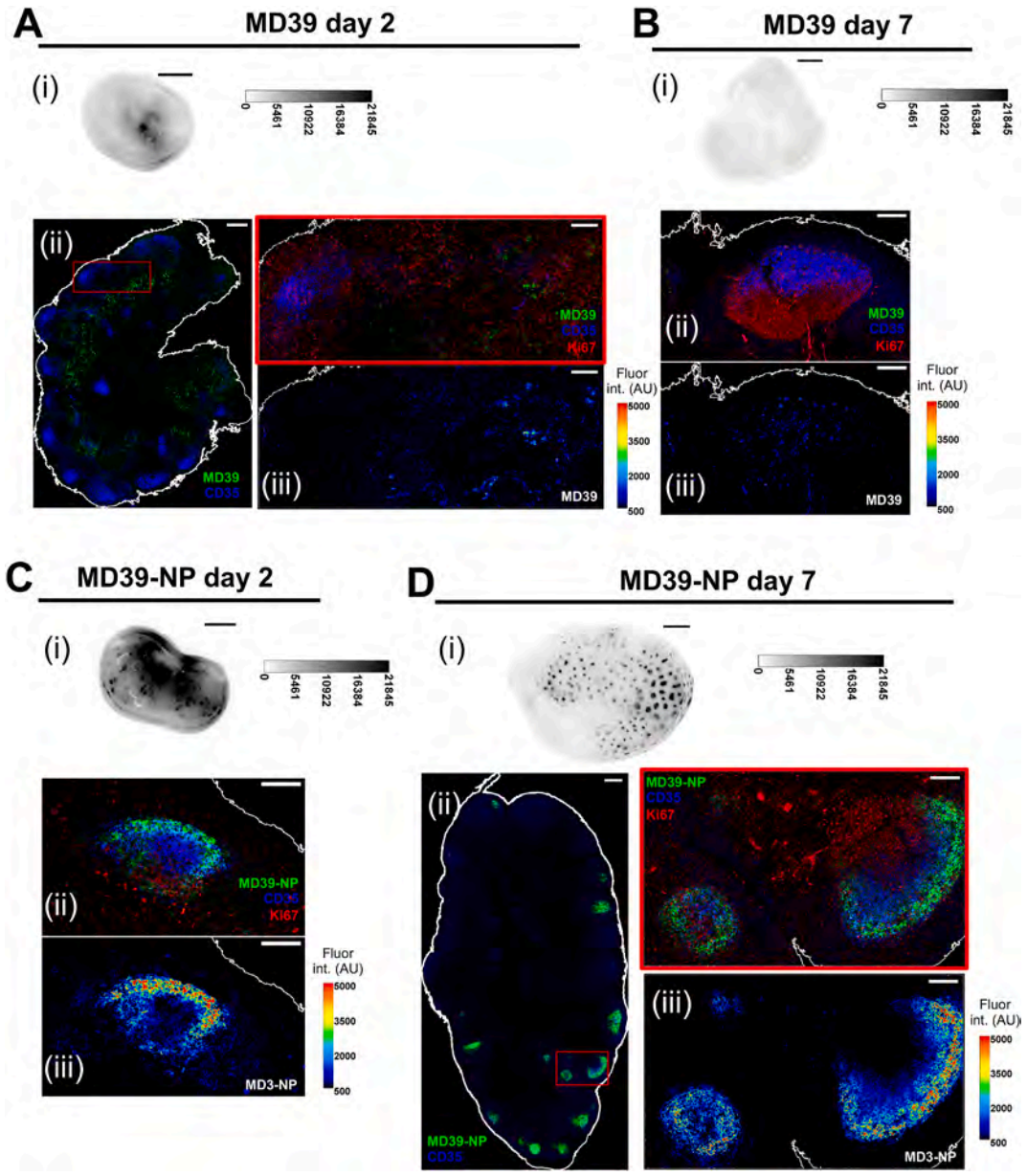

Fig. 5. Env trimer nanoparticles accumulate in the periphery of the FDC network of follicles while soluble Env trimer is dispersed through lymph nodes following primary immunization. (A–D) Representative lymph nodes positive for antigen signal were imaged by flatbed fluorescence scanner (i) and then sliced as 100 μm sections for confocal imaging. Shown are example whole slices or selected follicles (ii) and isolated antigen fluorescence channel in false color (iii). A) Iliac LN 2 days post immunization with MD39 trimer. Scale bars: (i) 2.5 mm, (ii) 1 mm, (iii) and inset 100 μm. B) Iliac LN 7 days post immunization with MD39 trimer. Scale bars: (i) 2.5 mm, (ii) and (iii) 100 μm. C) Iliac LN 2 days post immunization with MD39-NP. Scale bars: (i) 2.5 mm, (ii) and (iii) 100 μm. D) Iliac LN 7 days post immunization with MD39-NP. Scale bars: (i) 2.5 mm, (ii) 1 mm, (iii) and inset 100 μm. (For interpretation of the references to color in this figure legend, the reader is referred to the Web version of this article.)

have also been shown to be transported to the FDC network in mice mediated by antibody-triggered complement deposition [24,40], we hypothesized that even soluble Env trimers might exhibit concentration in follicles of animals that had pre-existing antibodies against the immunogen. To test this, we utilized a group of rhesus macaques that had previously been immunized three times with BG505 SOSIP Olio6$_{CD4\ KO}$ [14,41], a stabilized Env SOSIP trimer highly related in sequence to MD39. We first confirmed these animals had high levels of circulating IgG that recognized MD39 trimer by ELISA (Fig. S8). We anticipated that the presence of high antigen-specific antibody titers in these animals would lead to immediate immune complex formation upon injection of soluble MD39, and potentially induce follicular homing of the immunogen as observed with the MD39-NP. These animals were immunized with Alexa Fluor 647-labeled MD39 combined with saponin adjuvant and draining LNs were harvested 2 or 7 days post injection (Fig. 6A). Similar to the earlier studies, we analyzed antigen uptake in lymph nodes first by fluorescence scanner imaging of fixed tissues, followed by tissue clearing and whole-organ light sheet imaging.

As observed with the earlier experiments in naïve animals, substantial antigen signal accumulated in inguinal and iliac LNs by day 2. Fig. 6B shows quantified signal in animals that were previously immunized and boosted ('post-boost') compared to signal in naïve animals immunized only once with MD39 ('post-prime', i.e. soluble trimer data from Fig. 4B). At day 2, both post-prime and post-boost animals exhibited high levels of MD39 in iliac lymph nodes, while boosted animals also showed significant levels of antigen in inguinal LNs. Antigen

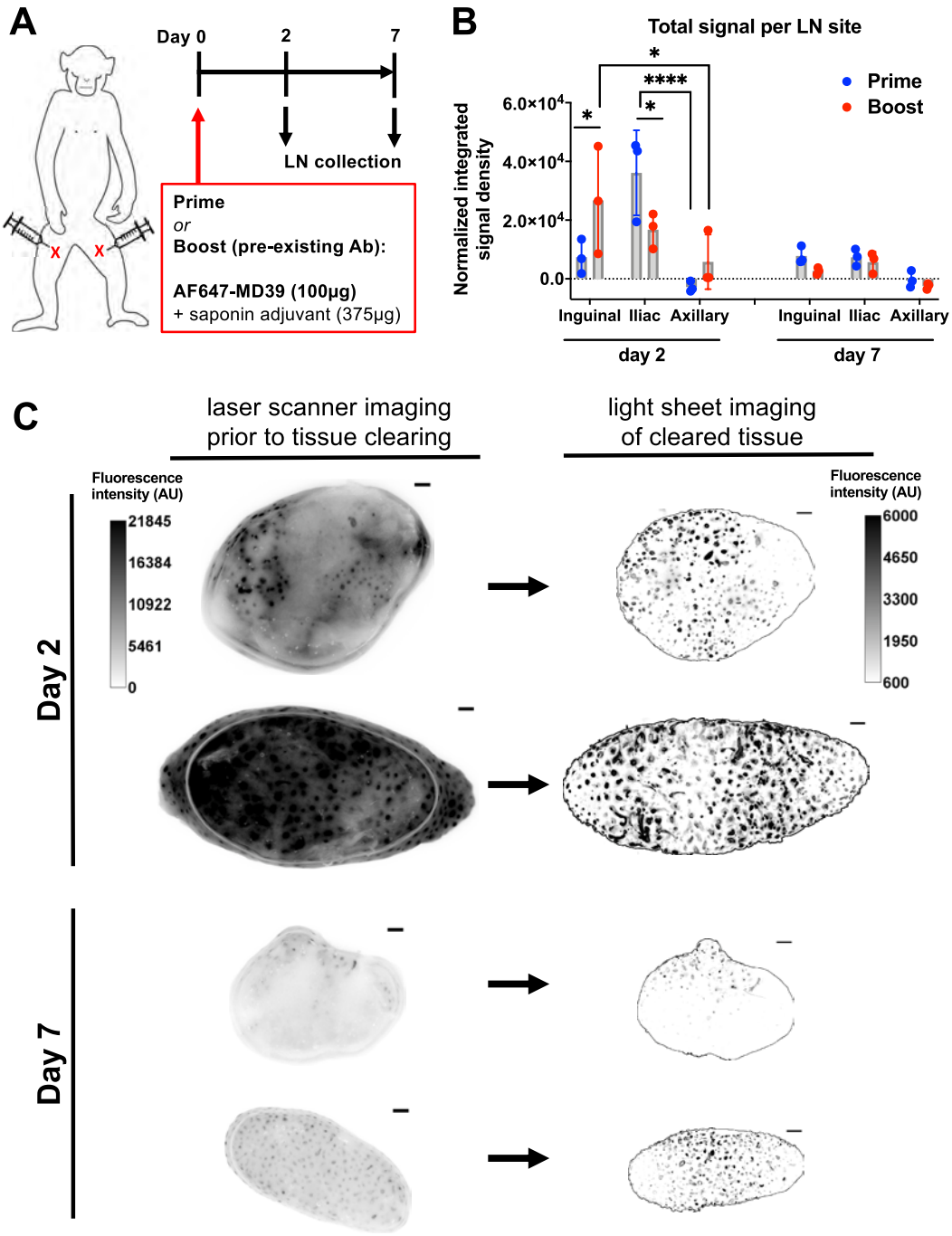

Fig. 6. Soluble Env trimer immunization in pre-immune animals leads to rapid antigen concentration in follicles. A) Immunization timeline: Rhesus macaques (n = 3/group) were primed or boosted on day 0 with a total dose of 100 μg AF647-MD39 + 375 μg saponin adjuvant, administered subcutaneously in both left and right upper inner thighs. Boost animals were previously immunized with BG505 SOSIP Olio6 and exhibited pre-existing circulating MD39-specific IgG. Animals were sacrificed and LNs collected two and seven days after immunization. B) Quantification of total fluorescent signal from fixed LNs at each collection site as measured using a fluorescent laser flatbed scanner. Dots represent pooled total fluorescence from one animal at the indicated site (minus naïve signal). Statistical significance determined by two-way ANOVA followed by Sidak's or Dunnett's post-hoc test (*$p < 0.05$, ****$p < 0.0001$). C) Comparison of LNs from MD39 boost animals before and after clarification, imaged by laser scanner (left) and light sheet microscopy (right), respectively. Light sheet microscopy images are maximum projections through an entire LN stack. Scale bars represent 1 mm.

levels in inguinal and iliac LNs decayed by day 7 but were still readily detectable above background (Fig. 6B). Whole-tissue images from the fluorescence scanner revealed that antigen-positive LNs from previously immunized animals, both 2 and 7 days post-boost with soluble trimer, were characterized by the same punctate pattern of antigen concentration previously observed only for MD39-NP (Fig. 6C). Antigen concentration in follicles was also revealed across entire lymph nodes by light sheet imaging of the cleared tissues in a pattern similar to that observed for MD39-NP, at both 2 and 7 days post-boost (Fig. 6C, Video S7). Thus, in agreement with findings from small animals, soluble HIV Env immunogens captured in immune complexes *in vivo* are also rapidly transported to B cell follicles.

Supplementary data related to this article can be found online at https://doi.org/10.1016/j.biomaterials.2021.120868

4. Discussion

The biodistribution of subunit vaccines at the organismal and tissue levels controls many facets of the outcome of immunization, influencing safety and magnitude of the immune response. Further, priming of T and B cell responses in lymphoid tissues draining mucosal sites programs homing of memory and plasma cells to the mucosal portals of pathogen entry [42]. For HIV, prior studies have suggested that vaccine delivery to iliac lymph nodes draining the genitourinary tract could lead to establishment of antigen-specific cytotoxic T cells in the vaginal and rectal tissues [43], and achieve enhanced protection from mucosal SIV challenge in macaques [10]. These findings are consistent with more recent analyses of lymphatic drainage in macaques suggesting that iliac lymph nodes drain the vaginal and rectal mucosa [29]. However, attempting to concentrate vaccine near deep iliac lymph nodes through needle injection is non-trivial.

These considerations motivated us to assess whether formulations that promote efficient trafficking of antigens/adjuvant into lymphatics could enable vaccine transport to key genitourinary tract-draining mucosal lymph nodes from an easily accessible subcutaneous injection site. Using a combination of whole animal PET and tissue-level fluorescence imaging in the rhesus macaque model, we assessed the impact of two distinct technology platforms for promoting lymph node targeting of vaccines, protein nanoparticles and albumin-binding molecular conjugates, on the fate of an HIV Env trimer immunogen and the molecular adjuvant CpG, respectively. Protein particles displaying antigen are being intensively studied for their capacity to enhance B cell triggering and augment the humoral immune response in preclinical models [27,44–48] and nanoparticle immunogens, including ferritin particles, are being assessed in humans (clinicaltrials.gov Identifiers: NCT03547245, NCT03186781, NCT04579250, NCT03814720). PET imaging revealed trafficking of both antigen and adjuvant to inguinal and iliac lymph nodes extending up the lymphatic chain from the injection site. Histology and whole cleared tissue imaging on individual lymph nodes in the drainage path revealed that while both Env nanoparticles and amph-CpG accumulated in draining lymph nodes, they exhibited very distinct distributions, with CpG distributing in the parenchyma and surrounding follicles, while the trimer NP immunogen exhibited a striking accumulation around the periphery of B cell follicles. Such follicular targeting was not detected for the equivalent soluble trimer in naïve animals, but was recapitulated in animals with pre-existing high levels of antigen-specific antibodies administered the soluble trimer.

Increasing the number of lymph nodes receiving a vaccine could be envisioned to enhance the immune response by allowing more independent germinal centers to develop and enabling antigen-specific cells to develop without intense competition for cytokines and other factors within a single lymph node. In small animals, lymph-targeted vaccines have been shown to distribute substantial distances through lymphatics (reaching from injection sites near the tail to axillary lymph nodes an entire body length away) [3,28], and small nanoparticles administered parenterally can reach the thoracic duct and hence the systemic circulation [49]. However, much less is known about vaccine biodistribution in larger animals closer in physiology to humans. In macaques, liposomal antigens and antigens administered with alum or oil-in-water emulsion adjuvants have been reported to exhibit a relatively restricted biodistribution following i. m. or s. c. immunization [50,51]: For example, when fluorescently-labeled liposomal Env antigens were administered s. c. over the quadriceps, histological analysis focused on the inguinal and iliac lymph nodes as the expected immediate primary and secondary draining sites revealed vaccine drainage almost exclusively to the inguinal LN, with no uptake in iliac nodes above background.

PET imaging is well suited to provide insight into vaccine trafficking as it combines high sensitivity, reasonable resolution, and very low background. A recent study analyzed the biodistribution of an mRNA vaccine expression in macaques, where mRNA encoding a PET reporter gene was complexed with cationic lipids to form ~320 nm diam. nanoparticles and administered in the quadriceps of macaques [52]. This analysis revealed transfected cells in the injection site, inguinal, iliac, and para-aortic lymph nodes at an early timepoint of 4 h, suggesting direct transfection of cells at these sites. The most distal lymph nodes reached by this vaccine were 9.2 cm away from the injection site. Similarly, in the present study PET imaging revealed the nanoparticle Env immunogen accumulated in numerous inguinal and iliac lymph nodes extending ~10 cm from the injection site. The albumin-binding CpG adjuvant trafficked further up the lymphatic chain, reaching lymph nodes 17 cm from the injection site. Antigen was largely undetectable outside of the draining lymphatic chain and immunization site. Variable numbers of lymph nodes are detected at each inguinal and iliac region in macaques, but we found significant vaccine uptake in at least half a dozen lymph nodes per animal. *Ex vivo* PET scanning greatly facilitated the identification and analysis of vaccine-positive lymph nodes during necropsies; ensuring that all lymph nodes are identified and isolated in a typical animal necropsy can be extremely challenging.

To allow tracking of MD39-NPs at the tissue level in parallel to whole-animal PET imaging, we mixed DOTA-labeled MD39-NPs with fluorophore-labeled particles to allow the dosing ratio of the PET agent and fluorescence tracer to be tightly controlled. This does raise the possibility that DOTA-labeled particles and fluorophore-labeled particles have somewhat different biodistributions due to the different labels used. However, as shown in Fig. S7C-D, the PET and fluorescence signals in lymph nodes for both MD39-NP and amph-CpG were highly correlated at the tissue level. Further, we have observed in our prior studies that fluorophore labeling did not alter the trafficking of ferritin nanoparticles in mouse lymph nodes [27], and hence we expect the labeling had minimal impact here.

Most notably, we observed that within individual lymph nodes, the Env trimer nanoparticle immunogen localized to dozens to hundreds of follicles, suggesting that antigen would be readily available to support ongoing germinal center reactions. We recently reported similar localization of the same ferritin-Env trimer particle immunogen to B cell follicles in mice, and showed this trafficking was driven by mannose binding lectin-mediated recognition of Env glycans and subsequent complement deposition on the particles [27]. A key question was whether follicular localization of such particulate immunogens would also be active in macaques, which are genetically much closer to humans, and how it would manifest in macaque lymphoid tissues that are much larger than mice and contain many more follicles. We recently reported initial findings with a two-component Env trimer protein nanoparticle, which exhibited follicular localization following vaccination in non-human primates [53]. Here we found that whole-tissue, cleared tissue, and histological imaging all showed that while soluble Env trimer was dispersed at low levels through the lymph node without notable localization in follicles, Env trimer-ferritin NP exhibited clear concentration in cup-like morphologies around many follicles in each lymph node (in many cases, exceeding 100 follicles). Preferential trafficking of the NP Env immunogen to follicles in naïve animals is consistent with a role for MBL-mediated recognition of these heavily glycosylated particles as observed in mice. This pattern of trimer accumulation was also observed when animals with pre-existing high levels of trimer-specific antibody were immunized with fluorescent soluble trimer. In the latter case, FDC trapping of antigen is expected to be mediated by immune complex (IC) formation and complement deposition on ICs, as described in mouse models [40]. This pattern of antigen accumulation mirrors our observations in a previous study where macaques were immunized with either slow-release osmotic pumps or through “extended dosing” immunization (where a given dose of vaccine is administered through injections spread over 2 weeks) [14]– we expect in these slow delivery immunizations that antigen capture on the FDC network is also mediated by IC formation.

5. Conclusions

Altogether, these results demonstrate that in large animals, subunit vaccines access a significant pool of lymph nodes from a common s. c. immunization site and can reach internal lymph nodes many cm away from the actual site of immunization within 24 h. Further, formulation of antigens in a nanoparticle form alters the trafficking of antigen within lymph nodes and can lead to pronounced accumulation in B cell follicles. Such follicular localization is associated with enhanced germinal center responses and the production of long-lived plasma cells in mice [27]. This follicular localization that was found to formally depend on mannose binding lectin-mediated recognition of dense glycosylation of the particulate immunogens in mice is relevant for diverse antigens ranging from HIV to influenza to SARS-CoV-2 [54], due to the prevalence of glycosylation on viral spike proteins that are important protective antigens.

Author contributions

JTM, BLH, RMR, WRS, SCK, DGC, DJI, PTF and GS designed the studies. WRS, SM, and TS provided immunogens for the studies. BLH prepared DOTA and fluorophore conjugates for PET and fluorescence imaging. SG and BG aided with radiochemistry and labeled sample preparation and analysis. SCK led PET and MRI measurements and tissue analysis, WZ and CGF assisted with PET/MRI and tissue analysis. DGC and GS led non-human primate immunizations at Emory University. JTM, BLH, MBM, BJC, JA, and TT carried out tissue analyses, histology, and confocal imaging. DJI, JTM, BLH, SCK, RMR, and WRS wrote the manuscript.

Credit author statement

Jacob T. Martin: Conceptualization, Investigation, Formal Analysis, Writing – Original draft. **Brittany L. Hartwell:** Conceptualization, Investigation, Formal Analysis, Writing – Original draft. **Sidath C. Kumarapperuma**: Conceptualization, Investigation, Formal Analysis, Writing – Original draft. **Mariane B. Melo:** Investigation. **Diane G. Carnathan:** Investigation, Writing – Review & Editing. **Benjamin J. Cossette:** Investigation. **Josetta Adams:** Investigation. **Siqi Gong:** Investigation. **Wei Zhang:** Investigation, Data Curation. **Talar Tokatlian:** Investigation. **Sergey Menis:** Resources. **Torben Schiffner:** Resources. **Crystal G. Franklin:** Investigation, Data Curation. **Beth Goins:** Investigation, Formal Analysis. **Peter T. Fox:** Supervision. **Guido Silvestri:** Supervision, Writing – Review & Editing. **William R. Schief:** Resources, Fundraising, Supervision, Writing – Review & Editing. **Ruth M. Ruprecht:** Resources, Fundraising, Supervision, Writing – Review & Editing. **Darrell J. Irvine:** Fundraising, Supervision, Project administration, Writing – Original draft.

Data availability

The data that support the findings of this study are available from the corresponding author upon reasonable request.

Declaration of competing interest

The authors declare that they have no known competing financial interests or personal relationships that could have appeared to influence the work reported in this paper.

Acknowledgments

This work was supported by the NIH (award P01AI048240 to RMR, SCK, PTF, and DJI, award UM1 AI144462 to DJI and WRS), the Ragon Institute of MGH, MIT, and Harvard, the U. S. Army Research Office through the Institute for Soldier Nanotechnologies at MIT, under Cooperative Agreement Number W911NF-18-2-0048, and the Koch Institute Support (core) Grant P30-CA14051.

Appendix A. Supplementary data

Supplementary data to this article can be found online at doi:10.1016/j.biomaterials.2021.120868.

References

[1] D. Baumjohann, S. Preite, A. Reboldi, F. Ronchi, K.M. Ansel, A. Lanzavecchia, F. Sallusto, Persistent antigen and germinal center B cells sustain T follicular helper cell responses and phenotype, Immunity 38 (2013) 596–605, https://doi.org/10.1016/j.immuni.2012.11.020.

[2] H.H. Tam, M.B. Melo, M. Kang, J.M. Pelet, V.M. Ruda, M.H. Foley, J.K. Hu, S. Kumari, J. Crampton, A.D. Baldeon, R.W. Sanders, J.P. Moore, S. Crotty, R. Langer, D.G. Anderson, A.K. Chakraborty, D.J. Irvine, Sustained antigen availability during germinal center initiation enhances antibody responses to vaccination, in: Proceedings of the National Academy of Sciences of the United States Of America, vol. 113, 2016, pp. E6639–E6648, https://doi.org/10.1073/pnas.1606050113.

[3] H. Liu, K.D. Moynihan, Y. Zheng, G.L. Szeto, A.V. Li, B. Huang, D.S.V. Egeren, C. Park, D.J. Irvine, Structure-based programming of lymph-node targeting in molecular vaccines, Nature (2014) 1–15, https://doi.org/10.1038/nature12978.

[4] J.R. Mora, M.R. Bono, N. Manjunath, W. Weninger, L.L. Cavanagh, M. Rosemblatt, U.H. von Andrian, Selective imprinting of gut-homing T cells by Peyer's patch dendritic cells, Nature 424 (2003) 88–93, https://doi.org/10.1038/nature01726.

[5] A. Habtezion, L.P. Nguyen, H. Hadeiba, E.C. Butcher, Leukocyte trafficking to the small intestine and colon, Gastroenterology 150 (2018) 1–15, https://doi.org/10.1053/j.gastro.2015.10.046.

[6] V. Mani, S.K. Bromley, T. Äijö, R. Mora-Buch, E. Carrizosa, R.D. Warner, M. Hamze, D.R. Sen, A.Y. Chasse, A. Lorant, J.W. Griffith, R.A. Rahimi, C.P. McEntee, K. L. Jeffrey, F. Marangoni, M.A. Travis, A. Lacy-Hulbert, A.D. Luster, T.R. Mempel, Migratory DCs activate TGF-β to precondition naïve CD8 +T cells for tissue-resident memory fate, Science 366 (2019), https://doi.org/10.1126/science.aav5728 eaav5728-15.

[7] A. Reboldi, T.I. Arnon, L.B. Rodda, A. Atakilit, D. Sheppard, J.G. Cyster, IgA production requires B cell interaction with subepithelial dendritic cells in Peyer's patches, Science 352 (2016), https://doi.org/10.1126/science.aaf4822 aaf4822–aaf4822.

[8] A.-Y. Lee, S.-Y. Chang, J.-I. Kim, H.-R. Cha, M.H. Jang, M. Yamamoto, M.-N. Kweon, Dendritic cells in colonic patches and iliac lymph nodes are essential in mucosal IgA induction following intrarectal administrationvia CCR7 interaction, Eur. J. Immunol. 38 (2008) 1127–1137, https://doi.org/10.1002/eji.200737442.

[9] H. Tezuka, Y. Abe, J. Asano, T. Sato, J. Liu, M. Iwata, T. Ohteki, Prominent role for plasmacytoid dendritic cells in mucosal T cell-independent IgA induction, Immunity 34 (2011) 247–257, https://doi.org/10.1016/j.immuni.2011.02.002.

[10] T. Lehner, Y. Wang, M. Cranage, L.A. Bergmeier, E. Mitchell, L. Tao, G. Hall, M. Dennis, N. Cook, R. Brookes, L. Klavinskis, I. Jones, C. Doyle, R. Ward, Protective mucosal immunity elicited by targeted iliac lymph node immunization with a subunit SIV envelope and core vaccine in macaques, Nat. Med. 2 (1996) 767–775.

[11] J.G. Cyster, B cell follicles and antigen encounters of the third kind, Nat. Immunol. 11 (2010) 989–996, https://doi.org/10.1038/ni.1946.

[12] S.F. Gonzalez, V. Lukacs-Kornek, M.P. Kuligowski, L.A. Pitcher, S.E. Degn, Y.-A. Kim, M.J. Cloninger, L. Martinez-Pomares, S. Gordon, S.J. Turley, M.C. Carroll, Capture of influenza by medullary dendritic cells via SIGN-R1 is essential for humoral immunity in draining lymph nodes, Nat. Immunol. 11 (2010) 427–434, https://doi.org/10.1038/ni.1856.

[13] R. Roozendaal, T.R. Mempel, L.A. Pitcher, S.F. Gonzalez, A. Verschoor, R. E. Mebius, U.H. von Andrian, M.C. Carroll, Conduits mediate transport of low-molecular-weight antigen to lymph node follicles, Immunity 30 (2009) 264–276, https://doi.org/10.1016/j.immuni.2008.12.014.

[14] K.M. Cirelli, D.G. Carnathan, B. Nogal, J.T. Martin, O.L. Rodriguez, A.A. Upadhyay, C.A. Enemuo, E.H. Gebru, Y. Choe, F. Viviano, C. Nakao, M.G. Pauthner, S. Reiss, C.A. Cottrell, M.L. Smith, R. Bastidas, W. Gibson, A.N. Wolabaugh, M.B. Melo, B. Cossette, V. Kumar, N.B. Patel, T. Tokatlian, S. Menis, D.W. Kulp, D.R. Burton, B. Murrell, W.R. Schief, S.E. Bosinger, A.B. Ward, C.T. Watson, G. Silvestri, D. J. Irvine, S. Crotty, Slow delivery immunization enhances HIV neutralizing antibody and germinal center responses via modulation of immunodominance, Cell 177 (2019), https://doi.org/10.1016/j.cell.2019.04.012, 1153-1171.e28.

[15] S.P. Kasturi, I. Skountzou, R.A. Albrecht, D. Koutsonanos, T. Hua, H.I. Nakaya, R. Ravindran, S. Stewart, M. Alam, M. Kwissa, F. Villinger, N. Murthy, J. Steel, J. Jacob, R.J. Hogan, A. García-Sastre, R. Compans, B. Pulendran, Programming the magnitude and persistence of antibody responses with innate immunity, Nature 470 (2011) 543–547, https://doi.org/10.1038/nature09737.

[16] N.L. Trevaskis, L.M. Kaminskas, C.J.H. Porter, From sewer to saviour — targeting the lymphatic system to promote drug exposure and activity, Nat. Rev. Drug Discov. 14 (2015) 781–803, https://doi.org/10.1038/nrd4608.

[17] A. Schudel, D.M. Francis, S.N. Thomas, Material design for lymph node drug delivery, Nat. Rev. Mater. 293 (2019) 1–14, https://doi.org/10.1038/s41578-019-0110-7.

[18] J. Marcandalli, B. Fiala, S. Ols, M. Perotti, W. de van der Schueren, J. Snijder, E. Hodge, M. Benhaim, R. Ravichandran, L. Carter, W. Sheffler, L. Brunner, M. Lawrenz, P. Dubois, A. Lanzavecchia, F. Sallusto, K.K. Lee, D. Veesler, C. E. Correnti, L.J. Stewart, D. Baker, K. Loré, L. Perez, N.P. King, Induction of potent neutralizing antibody responses by a designed protein nanoparticle vaccine for respiratory syncytial virus, Cell 176 (2019), https://doi.org/10.1016/j.cell.2019.01.046, 1420-1431.e17.

[19] G.M. Lynn, C. Sedlik, F. Baharom, Y. Zhu, R.A. Ramirez-Valdez, V.L. Coble, K. Tobin, S.R. Nichols, Y. Itzkowitz, N. Zaidi, J.M. Gammon, N.J. Blobel, J. Denizeau, P. Rochere, B.J. Francica, B. Decker, M. Maciejewski, J. Cheung, H. Yamane, M.G. Smelkinson, J.R. Francica, R. Laga, J.D. Bernstock, L.W. Seymour, C.G. Drake, C.M. Jewell, O. Lantz, E. Piaggio, A.S. Ishizuka, R.A. Seder, Peptide–TLR-7/8a conjugate vaccines chemically programmed for nanoparticle self-assembly enhance CD8 T-cell immunity to tumor antigens, Nat. Biotechnol. 38 (2020) 1–19, https://doi.org/10.1038/s41587-019-0390-x.

[20] V. Manolova, A. Flace, M. Bauer, K. Schwarz, P. Saudan, M.F. Bachmann, Nanoparticles target distinct dendritic cell populations according to their size, Eur. J. Immunol. 38 (2008) 1404–1413, https://doi.org/10.1002/eji.200737984.

[21] S. Reddy, A. van der Vlies, E. Simeoni, V. Angeli, G. Randolph, C. O'Neil, L. Lee, M. Swartz, J. Hubbell, Exploiting lymphatic transport and complement activation in nanoparticle vaccines, vol. 5, 2007, pp. 1159–1164.

[22] T.J. Moyer, Y. Kato, W. Abraham, J.Y.H. Chang, D.W. Kulp, N. Watson, H. L. Turner, S. Menis, R.K. Abbott, J.N. Bhiman, M.B. Melo, H.A. Simon, S.H.-D. la Mata, S. Liang, G. Seumois, Y. Agarwal, N. Li, D.R. Burton, A.B. Ward, W.R. Schief, S. Crotty, D.J. Irvine, Engineered immunogen binding to alum adjuvant enhances humoral immunity, Nat. Med. 26 (2020) 1–33, https://doi.org/10.1038/s41591-020-0753-3.

[23] T.Y.-H. Wu, M. Singh, A.T. Miller, E.D. Gregorio, F. Doro, U. D'Oro, D.A. G. Skibinski, M.L. Mbow, S. Bufali, A.E. Herman, A. Cortez, Y. Li, B.P. Nayak, E. Tritto, C.M. Filippi, G.R. Otten, L.A. Brito, E. Monaci, C. Li, S. Aprea, S. Valentini, S. Calabró, D. Laera, B. Brunelli, E. Caproni, P. Malyala, R.G. Panchal, T.K. Warren, S. Bavari, D.T. O'Hagan, M.P. Cooke, N.M. Valiante, Rational design of small molecules as vaccine adjuvants, Sci. Transl. Med. 6 (2014), https://doi.org/10.1126/scitranslmed.3009980, 263ra160-263ra160.

[24] A. Link, F. Zabel, Y. Schnetzler, A. Titz, F. Brombacher, M.F. Bachmann, Innate Immunity Mediates Follicular Transport of Particulate but not soluble Protein Antigen, vol. 188, 2012, pp. 3724–3733, https://doi.org/10.4049/jimmunol.1103312.

[25] Y.-N. Zhang, J. Lazarovits, W. Poon, B. Ouyang, L.N.M. Nguyen, B.R. Kingston, W. C.W.C.O. 0000-0001-5435-4785, nanoparticle size influences antigen retention and presentation in lymph node follicles for humoral immunity, Nano Lett. 19 (2019) 1–10, https://doi.org/10.1021/acs.nanolett.9b02834.

[26] C. Park, J. Arthos, C. Cicala, J.H. Kehrl, The HIV-1 envelope protein gp120 is captured and displayed for B cell recognition by SIGN-R1(+) lymph node macrophages, ELife 4 (2015), e06467, https://doi.org/10.7554/elife.06467.

[27] T. Tokatlian, B.J. Read, C.A. Jones, D.W. Kulp, S. Menis, J.Y.H. Chang, J. M. Steichen, S. Kumari, J.D. Allen, E.L. Dane, A. Liguori, M. Sangesland, D. Lingwood, M. Crispin, W.R. Schief, D.J. Irvine, Innate immune recognition of glycans targets HIV nanoparticle immunogens to germinal centers, Science 363 (2019), eaat9120, https://doi.org/10.1126/science.aat9120.

[28] K.D. Moynihan, R.L. Holden, N.K. Mehta, C. Wang, M.R. Karver, J. Dinter, S. Liang, W. Abraham, M.B. Melo, A.Q. Zhang, N. Li, S.L. Gall, B.L. Pentelute, D.J. Irvine, Enhancement of peptide vaccine immunogenicity by increasing lymphatic drainage and boosting serum stability, Canc. Immunol. Res. 6 (2018) 1025–1038, https://doi.org/10.1158/2326-6066.cir-17-0607.

[29] J. Smedley, B. Turkbey, M.L. Bernardo, G.Q.D. Prete, J.D. Estes, G.L. Griffiths, H. Kobayashi, P.L. Choyke, J.D. Lifson, B.F. Keele, Tracking the luminal exposure and lymphatic drainage pathways of intravaginal and intrarectal inocula used in nonhuman primate models of HIV transmission, PloS One 9 (2014), e92830, https://doi.org/10.1371/journal.pone.0092830.

[30] J.M. Park, C. Charnsangavej, K. Yoshimitsu, D.H. Herron, T.J. Robinson, S. Wallace, Pathways of nodal metastasis from pelvic tumors: CT demon- stration1, Radiographics 14 (1994) 1309–1321, https://doi.org/10.1148/radiographics.14.6.7855343.

[31] D. Sok, B. Briney, J.G. Jardine, D.W. Kulp, S. Menis, M. Pauthner, A. Wood, E. C. Lee, K.M. Le, M. Jones, A. Ramos, O. Kalyuzhniy, Y. Adachi, M. Kubitz, S. MacPherson, A. Bradley, G.A. Friedrich, W.R. Schief, D.R. Burton, Priming HIV-1 Broadly Neutralizing Antibody Precursors in Human Ig Loci Transgenic Mice, Science, New York, NY, 2016, pp. 1–10, https://doi.org/10.1126/science.aah3945.

[32] J.M. Steichen, D.W. Kulp, T. Tokatlian, A. Escolano, P. Dosenovic, R.L. Stanfield, L. E. McCoy, G. Ozorowski, X. Hu, O. Kalyuzhniy, B. Briney, T. Schiffner, F. Garces, N. T. Freund, A.D. Gitlin, S. Menis, E. Georgeson, M. Kubitz, Y. Adachi, M. Jones, A. A. Mutafyan, D.S. Yun, C.T. Mayer, A.B. Ward, D.R. Burton, I.A. Wilson, D.J. Irvine, M.C. Nussenzweig, W.R. Schief, HIV vaccine design to target germline precursors of glycan-dependent broadly neutralizing antibodies, Immunity (2016) 1–15, https://doi.org/10.1016/j.immuni.2016.08.016.

[33] N. Renier, Z. Wu, D.J. Simon, J. Yang, P. Ariel, M. Tessier-Lavigne, iDISCO: a simple, rapid method to immunolabel large tissue samples for volume imaging, Cell 159 (2014) 896–910, https://doi.org/10.1016/j.cell.2014.10.010.

[34] S.I. Kubota, K. Takahashi, J. Nishida, Y. Morishita, S. Ehata, K. Tainaka, K. Miyazono, H.R. Ueda, Whole-body profiling of cancer metastasis with single-cell resolution, Cell Rep. 20 (2017) 236–250, https://doi.org/10.1016/j.celrep.2017.06.010.

[35] D.J. Irvine, M.A. Swartz, G.L. Szeto, Engineering synthetic vaccines using cues from natural immunity, Nat. Mater. 12 (2013) 978–990, https://doi.org/10.1038/nmat3775.

[36] V.A. Stewart, S. McGrath, A.M. Krieg, N.S. Larson, E. Angov, C.L. Smith, T. G. Brewer, D.G. Heppner, Activation of innate immunity in healthy Macaca mulatta macaques by a single subcutaneous dose of GMP CpG 7909: safety data and interferon-inducible protein-10 kinetics for humans and macaques, Clin. Vaccine Immunol. 15 (2008) 221–226, https://doi.org/10.1128/cvi.00420-07.

[37] M. Kwissa, R.R. Amara, H.L. Robinson, B. Moss, S. Alkan, A. Jabbar, F. Villinger, B. Pulendran, Adjuvanting a DNA vaccine with a TLR9 ligand plus Flt 3 ligand results in enhanced cellular immunity against the simian immunodeficiency virus, J. Exp. Med. 204 (2007) 2733–2746, https://doi.org/10.1084/jem.20071211.

[38] C.L. Cooper, H.L. Davis, M.L. Morris, S.M. Efler, A.M. Krieg, Y. Li, C. Laframboise, M.J.A. Adhami, Y. Khaliq, I. Seguin, D.W. Cameron, Safety and immunogenicity of CPG 7909 injection as an adjuvant to Fluarix influenza vaccine, Vaccine 22 (2004) 3136–3143, https://doi.org/10.1016/j.vaccine.2004.01.058.

[39] A. Escolano, H.B. Gristick, M.E. Abernathy, J. Merkenschlager, R. Gautam, T. Y. Oliveira, J. Pai, A.P. West, C.O. Barnes, A.A. Cohen, H. Wang, J. Golijanin, D. Yost, J.R. Keeffe, Z. Wang, P. Zhao, K.-H. Yao, J. Bauer, L. Nogueira, H. Gao, A. V. Voll, D.C. Montefiori, M.S. Seaman, A. Gazumyan, M. Silva, A.T. McGuire, L. Stamatatos, D.J. Irvine, L. Wells, M.A. Martin, P.J. Bjorkman, M.C. Nussenzweig, Immunization expands B cells specific to HIV-1 V3 glycan in mice and macaques, Nature 570 (2019) 1–23, https://doi.org/10.1038/s41586-019-1250-z.

[40] T.G. Phan, I. Grigorova, T. Okada, J.G. Cyster, Subcapsular encounter and complement-dependent transport of immune complexes by lymph node B cells, Nat. Immunol. 8 (2007) 992–1000, https://doi.org/10.1038/ni1494.

[41] D.W. Kulp, J.M. Steichen, M. Pauthner, X. Hu, T. Schiffner, A. Liguori, C.A. Cottrell, C. Havenar-Daughton, G. Ozorowski, E. Georgeson, O. Kalyuzhniy, J.R. Willis, M. Kubitz, Y. Adachi, S.M. Reiss, M. Shin, N. Val, A.B. Ward, S. Crotty, D.R. Burton, W.R. Schief, Structure-based design of native-like HIV-1 envelope trimers to silence non-neutralizing epitopes and eliminate CD4 binding, Nat. Commun. 8 (2017) 1–14, https://doi.org/10.1038/s41467-017-01549-6.

[42] N. Lycke, Recent progress in mucosal vaccine development: potential and limitations, Nat. Rev. Immunol. 12 (2012) 592–605, https://doi.org/10.1038/nri3251.

[43] L.S. Klavinskis, L.A. Bergmeier, L. Gao, E. Mitchell, R.G. Ward, G. Layton, R. Brookes, N.J. Meyers, T. Lehner, Mucosal or targeted lymph node immunization of macaques with a particulate SIVp27 protein elicits virus-specific CTL in the genito-rectal mucosa and draining lymph nodes, J. Immunol. (Baltimore, Md? 157 (1950) 2521–2527, 1996.

[44] P.J.M. Brouwer, A. Antanasijevic, Z. Berndsen, A. Yasmeen, B. Fiala, T.P.L. Bijl, I. Bontjer, J.B. Bale, W. Sheffler, J.D. Allen, A. Schorcht, J.A. Burger, M. Camacho, D. Ellis, C.A. Cottrell, A.-J. Behrens, M. Catalano, I. del Moral-Sánchez, T.J. Ketas, C. Labranche, M.J. van Gils, K. Sliepen, L.J. Stewart, M. Crispin, D.C. Montefiori, D. Baker, J.P. Moore, P.-J. Klasse, A.B. Ward, N.P. King, R.W. Sanders, Enhancing and shaping the immunogenicity of native-like HIV-1 envelope trimers with a two-component protein nanoparticle, Nat. Commun. 10 (2019) 1–17, https://doi.org/10.1038/s41467-019-12080-1.

[45] J.G. Jardine, T. Ota, D. Sok, M. Pauthner, D.W. Kulp, O. Kalyuzhniy, P.D. Skog, T. C. Thinnes, D. Bhullar, B. Briney, S. Menis, M. Jones, M. Kubitz, S. Spencer, Y. Adachi, D.R. Burton, W.R. Schief, D. Nemazee, HIV-1 VACCINES. Priming a Broadly Neutralizing Antibody Response to HIV-1 Using a Germline-Targeting Immunogen, vol. 349, Science, New York, NY, 2015, pp. 156–161, https://doi.org/10.1126/science.aac5894.

[46] M. Kanekiyo, M.G. Joyce, R.A. Gillespie, J.R. Gallagher, S.F. Andrews, H. M. Yassine, A.K. Wheatley, B.E. Fisher, D.R. Ambrozak, A. Creanga, K. Leung, E. S. Yang, S. Boyoglu-Barnum, I.S. Georgiev, Y. Tsybovsky, M.S. Prabhakaran, H. Andersen, W.-P. Kong, U. Baxa, K.L. Zephir, J.E. Ledgerwood, R.A. Koup, P. D. Kwong, A.K. Harris, A.B. McDermott, J.R. Mascola, B.S. Graham, Mosaic nanoparticle display of diverse influenza virus hemagglutinins elicits broad B cell responses, Nat. Immunol. 20 (2019) 1–18, https://doi.org/10.1038/s41590-018-0305-x.

[47] K. Sliepen, G. Ozorowski, J.A. Burger, T. Montfort, M. Stunnenberg, C. Labranche, D.C. Montefiori, J.P. Moore, A.B. Ward, R.W. Sanders, Presenting native-like HIV-1 envelope trimers on ferritin nanoparticles improves their immunogenicity, Retrovirology 12 (2015) 1–5, https://doi.org/10.1186/s12977-015-0210-4.

[48] H.M. Yassine, J.C. Boyington, P.M. McTamney, C.-J. Wei, M. Kanekiyo, W.-P. Kong, J.R. Gallagher, L. Wang, Y. Zhang, M.G. Joyce, D. Lingwood, S.M. Moin, H. Andersen, Y. Okuno, S.S. Rao, A.K. Harris, P.D. Kwong, J.R. Mascola, G.J. Nabel, B.S. Graham, Hemagglutinin-stem nanoparticles generate heterosubtypic influenza protection, Nat. Med. 21 (2015) 1065–1070, https://doi.org/10.1038/nm.3927.

[49] I.C. Kourtis, S. Hirosue, A. de Titta, S. Kontos, T. Stegmann, J.A. Hubbell, M. A. Swartz, Peripherally administered nanoparticles target monocytic myeloid cells, secondary lymphoid organs and tumors in mice, PloS One 8 (2013), e61646, https://doi.org/10.1371/journal.pone.0061646.

[50] S. Ols, L. Yang, E.A. Thompson, P. Pushparaj, K. Tran, F. Liang, A. Lin, B. Eriksson, G.B.K. Hedestam, R.T. Wyatt, K. Loré, Route of vaccine administration alters antigen trafficking but not innate or adaptive immunity, Cell Rep. 30 (2020), https://doi.org/10.1016/j.celrep.2020.02.111, 3964-3971.e7.

[51] F. Liang, G. Lindgren, K.J. Sandgren, E.A. Thompson, J.R. Francica, A. Seubert, E. D. Gregorio, S. Barnett, D.T. O'Hagan, N.J. Sullivan, R.A. Koup, R.A. Seder, K. Loré, Vaccine priming is restricted to draining lymph nodes and controlled by adjuvant-mediated antigen uptake, Sci. Transl. Med. 9 (2017), https://doi.org/10.1126/scitranslmed.aal2094.

[52] K.E. Lindsay, S.M. Bhosle, C. Zurla, J. Beyersdorf, K.A. Rogers, D. Vanover, P. Xiao, M.A. x000Ed nga, L.M. Shirreff, B. Pitard, P. Baumhof, F. Villinger, P.J. Santangelo, Visualization of early events in mRNA vaccine delivery in non-human primates via

PET–CT and near-infrared imaging, Nat. Biomed. Eng. 196 (2019) 1–13, https://doi.org/10.1038/s41551-019-0378-3.

[53] J.T. Martin, C.A. Cottrell, A. Antanasijevic, D.G. Carnathan, B.J. Cossette, C. A. Enemuo, E.H. Gebru, Y. Choe, F. Viviano, S. Fischinger, T. Tokatlian, K. M. Cirelli, G. Ueda, J. Copps, T. Schiffner, S. Menis, G. Alter, W.R. Schief, S. Crotty, N.P. King, D. Baker, G. Silvestri, A.B. Ward, D.J. Irvine, Targeting HIV Env immunogens to B cell follicles in nonhuman primates through immune complex or protein nanoparticle formulations, Npj Vacc. 5 (2020) 72, https://doi.org/10.1038/s41541-020-00223-1.

[54] Y. Watanabe, J.D. Allen, D. Wrapp, J.S. McLellan, M. Crispin, Site-specific glycan analysis of the SARS-CoV-2 spike, Science 369 (2020) 330–333, https://doi.org/10.1126/science.abb9983.